

# Transmon qutrit-based simulation of spin-1 AKLT systems

Keerthi Kumaran,<sup>1,2</sup> Faisal Alam,<sup>3,4</sup> Norhan Eassa,<sup>1,2</sup> Kaelyn Ferris,<sup>5</sup>  
Xiao Xiao,<sup>6,2</sup> Lukasz Cincio,<sup>3,2</sup> Nicholas Bronn,<sup>5</sup> and Arnab Banerjee<sup>1,2</sup>

<sup>1</sup>*Department of Physics and Astronomy, Purdue University, West Lafayette, IN 47907, USA*

<sup>2</sup>*Quantum Science Center, Oak Ridge National Laboratory, Oak Ridge, TN 37831, USA*

<sup>3</sup>*Theoretical Division, Los Alamos National Laboratory, Los Alamos, NM 87545, USA*

<sup>4</sup>*Department of Physics, University of Illinois at Urbana-Champaign, IL 61801, USA*

<sup>5</sup>*IBM Quantum, IBM T.J. Watson Research Center, Yorktown Heights, New York 10598, USA*

<sup>6</sup>*North Eastern University, Boston, MA 02115, USA*

Qutrit-based quantum circuits could help reduce the overall circuit depths, and hence the noise, when the system of interest has local dimension of three. Accessing second excited states in superconducting transmons provides a straightforward hardware realization of three-level systems, or qutrits, useful for such ternary encoding. In this work, we successfully calibrate pulse gates to a low error rate to obtain transmon qutrits. We use these qutrits to simulate one-dimensional spin-1 AKLT states (Affleck, Lieb, Kennedy, and Tasaki) which exhibit a multitude of interesting phenomena such as topologically protected ground states, string order and the existence of a robust Berry phase. We demonstrate the efficacy of qutrit-based simulation by preparing high-fidelity ground states of the AKLT Hamiltonian with open boundaries for various chain lengths. We then use ground state preparations of the perturbed AKLT Hamiltonian with periodic boundaries to calculate the Berry phase and illustrate non-trivial ground state topology. We further present scalable methods for preparing the AKLT state and computing its Berry phase, and use tensor network simulations to establish the advantage of qutrit-based implementation over qubit-based ones in the presence of noise. Our work provides a pathway toward more general spin-1 physics simulations using transmon qutrits, with applications in chemistry, magnetism, and topological phases of matter.

## I. INTRODUCTION

Noisy Intermediate-Scale Quantum (NISQ) [1] computers have reached a point where they are actively being used in simulating physical systems. These simulations on quantum hardware are becoming increasingly impactful as they reach utility in simulating large-scale systems [2–6]. While these simulations predominantly utilize qubit-based encoding schemes, simulation of higher spin systems (e.g. [7–10]) is difficult to realize efficiently. This is because encoding a higher spin ( $s > 1/2$ ) requires multiple qubits. In addition to the encoding complexity, qubit-based schemes might also be more affected by noise because they inherently require more qubits than the number of spins in the system we wish to study and likely involve deeper and hence noisier circuits.

Qudit ( $d$ -level) encoding schemes, which offer access to a larger computational space beyond two levels, have demonstrated advantages in various applications such as error correction ([11, 12]), quantum key distribution ([13, 14]), and in requiring fewer entangling gates in execution of certain algorithms like Shor’s [15], Grover’s [16], and the quantum Fourier transformation [17]. Similarly, qudit encoding schemes are better suited for simulating systems that are inherently based on  $d$  levels. On the theoretical front, studies aimed at developing tools for qutrit (three-level) simulations, such as algebraic relations for circuit compression and optimization to improve circuit fidelities [18], have been undertaken. Experimentally, significant advances have been made in implementing qutrits using superconducting transmons [19–21], photonic circuits [22], and trapped ions [23, 24]. These experimental realizations have led to the development of high-fidelity multi-qubit gates [25] and maxi-

mally entangled qutrit state preparation [26]. In a noise-free setup, one could continue gaining an advantage by accessing energy levels beyond the third level of transmons to encode higher spin systems. However, in real transmons, higher levels are affected by various channels of decoherence (see [26, 27]) and are unsuitable for encoding higher spin systems. As a result, we restrict our focus to qutrits in this work.

This study investigates the ground states of the well-known one-dimensional spin-1 AKLT Hamiltonian [28]. This Hamiltonian is one of the simplest symmetry-protected topological models (some others include [29–31]), providing numerous interesting physical phenomena such as the existence of string order [32] and robust Berry phase [33]. Under open boundary conditions (OBC), ground states host edge modes mimicking two free spin  $1/2$ s at the edges of the open chain and hence have a degeneracy of four. Previous work preparing ground state circuits utilized qubit-based encoding and dynamic circuits [34, 35]. These works rely on special properties of ground states of the AKLT model such as the possibility of representing them as valence bond states composed of qubits and the low bond dimension of their matrix product state (MPS) representation.

Recently, a trapped ions-based simulation of AKLT states was undertaken [36] aimed at finding the long-range string order of the OBC AKLT ground states. In this work, we utilize custom-calibrated microwave pulses (pulse gates) to access the second excited state of IBM Quantum transmons. By expanding the default qubit gate set to a qutrit gate set, we demonstrate a more straightforward method for preparing the ground states of the AKLT Hamiltonian. We achieve high-fidelity preparation of ground states for the AKLT

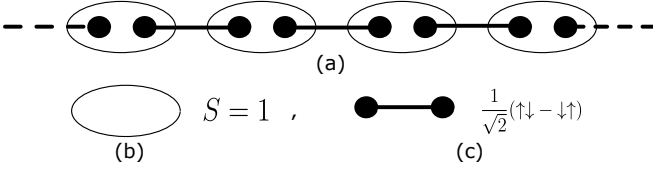


FIG. 1. In spin-1 systems, each spin-1 site can be represented by a tensor product of a pair of spin-1/2 sites (a & b) followed by their projection to the spin-1 sector. In AKLT ground states, these adjacent spin-1 sites decompose as pairs of two spin-1/2s (a & c) that form singlets (valence bond states) between them.

Hamiltonian with OBC across various chain lengths and under periodic boundary conditions (PBC) subjected to different degrees of perturbation for a fixed chain length. We compute a non-trivial Berry phase by applying these perturbations [37], providing crucial physical insights into the presence of valence bonds in the system.

The paper is structured as follows: we begin with a review of the AKLT model, highlighting its rich physical properties. Next, we examine the pulse-level calibration processes essential for constructing the qutrit gate set to be used. Using these custom-calibrated qutrit gates, we discuss the efficient ground state circuits for the OBC AKLT Hamiltonian and report their Hellinger fidelities. Following this, we prepare the ground states of the perturbed PBC AKLT Hamiltonian which can be faithfully characterized by Berry phases [38–40]. We then present scalable methods for preparing the AKLT state and computing its Berry phase and use tensor-network simulations to show the advantage of qutrit-based implementations over qubit-based ones in the presence of noise.

The discussion here can be easily adapted for other spin-1 systems. Hence, our qutrit-based encoding methods can be utilized to investigate a wider class of physically relevant quantities in spin-1 systems.

## II. REVIEW OF AKLT MODEL

The spin-1 AKLT Hamiltonian on a one-dimensional chain of length  $n$  is defined as [28]

$$H = \sum_{i=1}^n \vec{S}_i \cdot \vec{S}_{i+1} + \frac{1}{3} (\vec{S}_i \cdot \vec{S}_{i+1})^2, \quad (1)$$

where the spin-one operator is denoted by the vector operator  $\vec{S}_i = (S_i^x, S_i^y, S_i^z)$  with  $S_i^\alpha$  a spin-1 operator for the  $\alpha$ -component on the site  $i$ .

For open boundary conditions (OBC), the system has 4 degenerate ground states corresponding to the Hilbert space of two emergent free spin-1/2s at the edges. For periodic boundary conditions (PBC), the ground state is non-degenerate as there are no free edges and the ground state is composed of singlet pairs (valence bond states) in the bulk.

These localized valence bond states in the ground state are not unique to the AKLT Hamiltonian but are also known to occur in various  $S = 1, 2$  dimerized Heisenberg models and the  $S = 2$  Heisenberg chain with uniaxial single-ion-type anisotropy [41–43]. The presence of local valence bond states in the bulk gives rise to a non-trivial local Berry phase of  $\pi$ . It has been recently shown that this non-trivial Berry phase is obtained for any finite-size PBC AKLT chain [44]. We will discuss Berry phase computation using qutrit circuits in section VII.

The AKLT ground states (both OBC and PBC) also have straightforward matrix product state (MPS) representations. The OBC ground state in this representation has the form

$$|\Psi\rangle_{OBC} = \sum_{\sigma} (b_A^{\prime T} A^{\sigma_1} A^{\sigma_2} \dots A^{\sigma_N} b_A^r) |\sigma_1 \sigma_2 \dots \sigma_N\rangle \quad (2)$$

and for the PBC ground state we have,

$$|\Psi\rangle_{PBC} = \sum_{\sigma} \text{Tr}[A^{\sigma_1} A^{\sigma_2} \dots A^{\sigma_N}] |\sigma_1 \sigma_2 \dots \sigma_N\rangle \quad (3)$$

where  $\sigma_i \in \{+, -, 0\}$  labels the  $i$ -th spin-1 basis state, with corresponding MPS matrices  $A^\sigma$  given by

$$A^+ = \sqrt{2/3}\tau^+, A^- = -\sqrt{2/3}\tau^-, A^0 = -\sqrt{1/3}\tau^z \quad (4)$$

where  $\tau^\pm = \tau^x \pm i\tau^y$  and  $\tau^z$  span the set of Pauli matrices. Note that for OBC, we have two boundary vectors  $b^r$  and  $b^l$  spanning the four-dimensional degenerate ground state subspace. These MPS representations play a crucial role in compiling scalable qutrit based ground state circuits as we will discuss in the section VI.

The Hilbert space of the chain  $(\mathbb{C}^3)^{\otimes n}$  can be represented by a tensor product of  $n$  symmetric subspaces composed of pairs of spin-1/2 sites. In this representation, the AKLT Hamiltonian is (up to an additive constant) a positive sum of  $S = 2$  projectors on neighboring sites. In the ground states, the spin-1 sites decompose as pairs of two spin-1/2s that form singlets (valence bond states) between neighboring sites (See Fig. 1) have zero support on such  $S = 2$  projectors and hence minimize the Hamiltonian. These spin-1/2 representations play a significant role in the previously studied qubit-based AKLT ground state preparation [34]. In this work, we seek to prepare high-fidelity ground states corresponding to the spin-1 representation of the MPS as defined in Eq. (2) & (3) using qutrit-based circuits. This is discussed in Sections IV & V.

## III. QUTRIT GATE SET

IBM Quantum transmons are multilevel systems (with states  $|0\rangle, |1\rangle, |2\rangle, \dots$ ) typically driven by microwave pulse

gates ( $X_{01}, \sqrt{X_{01}}$ ) at the ground state ( $|0\rangle$  state) to the first excited state ( $|1\rangle$  state) transition frequency. This allows encoding of a general normalized two-dimensional complex vector set  $\mathbf{B}$  in the  $0-1$  manifold as follows

$$\mathbf{B} = \{a_0 |0\rangle + a_1 |1\rangle, |a_0|^2 + |a_1|^2 = 1\} \quad (5)$$

The existence of anharmonicity in the IBM Quantum transmons results in the next transition frequency ( $|2\rangle$  to  $|1\rangle$ ) being slightly different compared to the  $|0\rangle$  to  $|1\rangle$  transition frequency. As a result, applying microwave pulse gates at the  $1-2$  frequency ( $X_{12}$  and  $\sqrt{X_{12}}$ ) will enable us to encode two-level systems in the  $1-2$  manifold. These  $1-2$  manifold pulse gates along with the default  $0-1$  manifold counterparts could be used to encode a general normalized three-dimensional complex vector set  $\mathbf{T}$  in the  $0-1-2$  manifold as follows

$$\mathbf{T} = \{a_0 |0\rangle + a_1 |1\rangle + a_2 |2\rangle, |a_0|^2 + |a_1|^2 + |a_2|^2 = 1\} \quad (6)$$

To prepare AKLT ground states, along with the default  $0-1$  manifold gate set containing  $X_{01}$ ,  $\sqrt{X_{01}}$ , virtual  $RZ_{01}$  gate [45], and the  $\text{CNOT}_{01}$  gate, we custom calibrate the single qutrit microwave pulse gates in the  $1-2$  manifold ( $X_{12}$  and  $\sqrt{X_{12}}$ ) and define a virtual  $RZ_{12}$  gate. We achieve this by using Qiskit Pulse which allows us to create microwave pulse gates of the required amplitude, frequency, and other shape parameters of the pulse [46].

We follow a calibration procedure to obtain high-fidelity gates in the  $1-2$  manifold, detailed further in Appendix D. After obtaining the reported anharmonicity from the IBM Quantum backend configuration, we obtain the  $1-2$  transition frequency by performing narrow-band spectroscopy around the estimated value. This is followed by continuous Rabi and Ramsey experiments to refine the pulse amplitudes of the  $X_{12}$  and  $\sqrt{X_{12}}$  gates and  $1-2$  transition frequency respectively (pulse durations are set to those of the  $X_{01}$  gates). These are further refined by error-amplified Rabi and Ramsey experiments [47] before a final DRAG calibration [48] to correct line dispersion and  $Z_{12}$  errors from the higher levels of the qutrit [49]. The fidelity of single-qutrit gates in the  $1-2$  manifold is then determined by randomized benchmarking [50] in the  $1-2$  manifold and reported in Table V.

#### IV. CIRCUITS FOR OBC AKLT GROUND STATES

To construct OBC AKLT ground state circuits, we utilize the qutrit gate set defined in the Section III. When compiling circuits for qutrits, it's important to recognize that the previously insignificant global phases ( $-i$ ) associated with the  $0-1$  manifold become significant. Consequently, their  $SU(3)$  matrix representation must be taken into account when compiling for qutrit circuits. See Refs. [25, 26] for related discussion. Refer to Appendix A for the matrix representations of the qutrit gate set used.

To benchmark the efficacy of qutrit-based encoding of the OBC AKLT states, we estimate the closeness of the probability vector of ground states from hardware and the exact probability vector by Hellinger fidelity computation (see Appendix B). Here, the probability vector refers to the square of the absolute value of the state vector components. We restrict our analysis to Hellinger fidelity instead of the quantum fidelity (Appendix B) because of the realness of the OBC AKLT ground states and the absence of significant phases in the state vector. This is unlike the perturbed PBC AKLT ground states where we perform post-selection-based state tomography and phase correction for the dominant components of the state vector as they are crucial in the Berry phase estimate.

To obtain the probability vector of the ground states from the hardware, our qutrit-based simulation requires a few additional steps. Qubit states could be measured using a highly accurate  $0-1$  discriminator that classifies  $|0\rangle$  state from  $|1\rangle$  state with a very low readout error (See Appendix C). The absence of a  $0-1-2$  discriminator for the IBM Quantum backends means that both the  $|1\rangle$  and  $|2\rangle$  get classified as  $|1\rangle$  state. So, to compute Hellinger fidelities, one needs additional circuits to get the probability of ternary bit strings. This procedure scales exponentially in the number of qutrits, as noted in [26]. In the Appendix D4, we show typical error rates of a simple custom-built  $0-1-2$  discriminator [51] of IBM Quantum transmons and relate it to the need for an exponential number of circuits relying only on the  $0-1$  discriminator for accurate fidelity computation. However, there are other successful efforts in building  $0-1-2$  discriminator [52]. Including that in our work should vastly reduce the number of circuits. The noisy simulations that we present are devoid of this discriminator-based deficiency and hence allow us to estimate fidelities for arbitrarily large system sizes.

A recursive schematic of obtaining the probability vector from the hardware, which distinguishes the  $|1\rangle$  states from  $|2\rangle$  states by bringing them to  $|0\rangle$  states, is described in Figure 2. Here, the probability vector  $\vec{P}_n(C_n)$  of a classical ternary  $n$ -bit string  $((c_1, c_2, \dots, c_n) = C_n)$  for a  $n$ -qutrit circuit is expressed in terms of the probabilities  $\vec{P}_{n-1, c_n=c}(C_{n-1})$  of a classical ternary  $(n-1)$  bit string  $((c_1, c_2, \dots, c_{n-1}) = C_{n-1})$  and  $c = 0$  or  $1$  corresponding to the first  $(n-1)$  qutrits of the original  $n$ -qutrit circuit with and without  $X_{01}$  gate appended on the  $n$ -th qutrit. The subscript indicates that we post select measurements where  $c_n = c$  ( $0$  or  $1$ ).

The base case of the recursive schematic involves computing the probabilities  $\vec{P}_1$  of the  $n = 1$  circuit with the raw probabilities  $P$  (classifying  $|0\rangle$  from  $|1\rangle$  and  $|2\rangle$  states) straightforwardly as follows:  $P_1(0) = P(0)$  of the single qutrit circuit; and  $P_1(1) = P(0)$  of the same circuit with  $X_{01}$  appended. Finally, with these two probabilities, one can obtain  $P_1(2) = 1 - P_1(0) - P_1(1)$ .

The recursive part of the schematic involves the following steps:

- $\vec{P}_n(C_{n-1}, c_n = 0) = \vec{P}_{n-1, c_n=0}(C_{n-1})$  of the original circuit.
- $\vec{P}_n(C_{n-1}, c_n = 1) = \vec{P}_{n-1, c_n=0}(C_{n-1})$  of the original circuit with  $X_{01}$  gate appended on the  $n$ -th qutrit
- $\vec{P}_n(C_{n-1}, c_n = 2) = \vec{P}_{n-1, c_n=1}(C_{n-1})$  of the original circuit  $-\vec{P}_n(C_{n-1}, c_n = 1)$ .

This recursion is followed to lower and lower system sizes until our base case, which corresponds to  $n = 1$ .

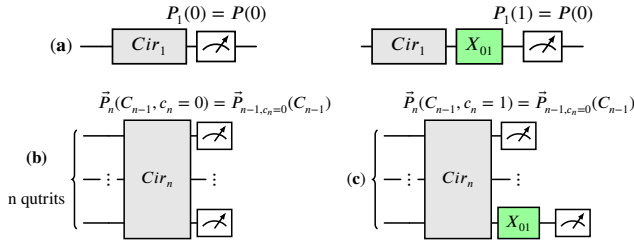


FIG. 2. **Schematic of constructing the probability vector ( $\vec{P}_n$ ) of qutrit circuit (b) from probabilities ( $\vec{P}_{n-1, c_n=c}$  of (b) and (c) where  $c_n = \{0, 1\}$ :** Let  $C_n$  be the sequence of classical ternary bits  $c_1, c_2, \dots, c_n$ . Then,  $\vec{P}_n(C_{n-1}, c_n = 0)$  of the circuit (b) equals  $\vec{P}_{n-1, c_n=0}(C_{n-1})$  of the same circuit (b).  $\vec{P}_n(C_{n-1}, c_n = 1)$  of the circuit (b) equals  $\vec{P}_{n-1, c_n=0}(C_{n-1})$  of the circuit (c). And  $\vec{P}_n(C_{n-1}, c_n = 2)$  of circuit (b) equals  $\vec{P}_{n-1, c_n=1}(C_{n-1})$  of circuit (b)  $-\vec{P}_n(C_{n-1}, c_n = 1)$ . This recursion on the number of qutrits is followed until the circuit has just one qutrit. At the level of one qutrit, in terms of raw probabilities  $P$ ,  $P_1(0) = P(0)$  of the first circuit in (a) and  $P_1(1) = P(0)$  of the second circuit in (a) and  $P_1(2) = 1 - P_1(0) - P_1(1)$ .

As noted in [26], working with higher-dimensional states would bring in additional channels of decoherence such as  $|2\rangle \rightarrow |1\rangle$  relaxation (T1 process), dephasing (T2), and aggravation of qubit crosstalk due to the inclusion of  $|2\rangle \rightarrow |1\rangle$  transition frequencies [26]. This leads us to consider circuits where we restrict all the possible  $0 - 1$  manifold operations ( $U_{01}(\phi)$  in Figs. 3, 4, 5) at the start of the circuit and reserve the qutrit pulse gates/operations ( $V(\theta)$ ) toward the end of the circuits. In the following section, we discuss such circuit ansatz that captures all four degenerate ground states of an OBC AKLT chain for chain lengths up to four while making sure that the effects of charge dispersion [27], decoherence from higher levels, and ac-Stark shifts due to higher levels (discussed in detail in section V A) are minimized. The fidelities are expected to be maximized without such considerations with the help of a scalable ground state ansatz described in section VI provided we have access to high-fidelity entangling qutrit pulse gates (as in, e.g., [53]).

### A. Circuit Ansatz

The circuit ansatz for chain lengths  $n = 2, 3, 4$  are depicted in Figs. 3, 4, 5. The  $U_{01}$  gates represent the default param-

eterized single qubit gates (see Appendix E). The  $V$  gate represents a parametrized sequence of pulse gates in the general  $0 - 1 - 2$  manifold. We refer the reader to the Appendix E for the exact sequence of gates.

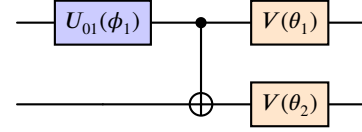


FIG. 3.  **$n = 2$  ansatz** capturing all four OBC ground states of  $n = 2$  AKLT. The exact parameters and sequence of pulse gates used in these single qubit gates can be found in the Appendix E.

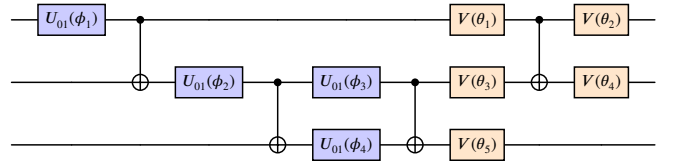


FIG. 4.  **$n = 3$  ansatz** capturing all the four OBC ground states of  $n = 3$  AKLT. The exact parameters and sequence of pulse gates used in these parameterized single qubit gates can be found in the Appendix E.

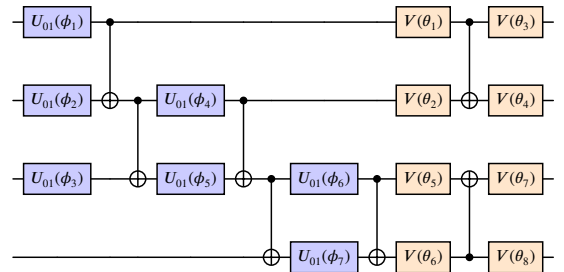


FIG. 5.  **$n = 4$  ansatz** capturing all four OBC ground states of  $n = 4$  AKLT. The exact parameters and sequence of pulse gates used in these parameterized single qubit gates can be found in the Appendix E.

The Hellinger fidelities of the OBC AKLT ground states are obtained with the help of the scheme in Fig. 2 and are listed in the table I. Note that only two states correspond to each  $n$ , this is because, for  $n = 2$ , one of the ground states is confined to  $0 - 1$  manifold and can be prepared without qutrit gates to  $\sim 99\% - 100\%$  Hellinger fidelity. For the other three ground states, circuits (2 a) and (2 b) along with  $X_{01}$  gates appended circuits (as described in Fig. 2) suffice for Hellinger fidelity computation. Similarly, circuits (3 a) and (3 b) and circuits (4 a) and (4 b) along with the  $X_{01}$  gates appended circuits suffice to compute the Hellinger fidelities of all the four ground states corresponding to  $n = 3$  and  $n = 4$  respectively.

n	State	CNOTs count	Hellinger fidelities
2	(2 a)	1	97.57%
2	(2 b)	1	98.36%
3	(3 a)	4	94.27%
3	(3 b)	4	96.99%
4	(4 a)	7	88.68%
4	(4 b)	7	80.80%

TABLE I. Hellinger fidelities of OBC AKLT ground states. The table contains circuits that are sufficient to compute the Hellinger fidelities of all four ground states corresponding to  $n = 2$ ,  $n = 3$ , and  $n = 4$ , except for the one ground state of  $n = 2$ , which is fully confined to the  $0-1$  manifold and has 99%–100% Hellinger fidelity. In the reported fidelities, we observe a drop in the values with the increase in chain lengths, an expected trend as noise accumulates with the increase in circuit depth.

We observe a drop in the Hellinger fidelities with the increase in chain lengths, an expected trend as noise accumulates with the increase in circuit depth. These results have been obtained without any additional error mitigation techniques. We expect to see improvements with schemes like dynamical decoupling focused on reducing the  $|2\rangle \rightarrow |1\rangle$  decay as explored in [25, 26]. More details regarding the exact states and additional circuits to compute the Hellinger fidelities along with the hardware data can be found in the GitHub repository linked in Appendix E.

## V. THE GROUND STATES OF PERTURBED AKLT HAMILTONIAN UNDER PERIODIC BOUNDARY CONDITIONS

We prepare the ground states of a locally perturbed AKLT Hamiltonian on a 1D qutrit chain under periodic boundary conditions (PBC). With the methods outlined in this section, we will be able to calculate a quantity known as the Berry phase which reveals the existence of valence bond states in the 1D PBC AKLT chains.

The Hamiltonian for a 1D chain of length  $n$  with periodic boundary conditions is expressed as follows

$$H = \sum_{i=1}^{n-1} \left( \vec{S}_i \cdot \vec{S}_{i+1} + \frac{1}{3} (\vec{S}_i \cdot \vec{S}_{i+1})^2 \right) + \left( \vec{S}_N \cdot \vec{S}_1 + \frac{1}{3} (\vec{S}_N \cdot \vec{S}_1)^2 \right). \quad (7)$$

In the PBC system represented by Eq. (7), a class of Hamiltonians can be defined by introducing local perturbations to the bond between the  $j$ -th and  $(j+1)$ -th sites. We modify the Hamiltonian for the perturbed bond as follows:

$$\vec{S}_j \cdot \vec{S}_{j+1} \rightarrow e^{i\theta} S_j^+ S_{j+1}^- / 2 + e^{-i\theta} S_j^- S_{j+1}^+ / 2 + S_j^z S_{j+1}^z, \quad (8)$$

where  $S_i^\pm = S_i^x \pm S_i^y$ . This perturbation, proposed in [37], is a local spin twist and leaves other bonds unchanged. This twist also introduces a generic parameter essential for computing

the Berry phase in AKLT-like systems.

It has been recently shown that any finite-length PBC AKLT chain shows a  $\pi$  Berry phase [44] for the perturbation described in Eq. (8). To demonstrate this on hardware, we prepare the perturbed ground states on chains of length 2 using ancilla-free ansatz (Fig. 7). With ancilla-free ground state circuits, we limit our focus to chains of length 2, unlike OBC because of the absence of closed-loop connectivity in hardware for general chain lengths. To prepare PBC ground states with ancilla-free ansatz for an arbitrary chain length, a series of CSWAP/SWAP gates are required in the circuit. This introduces additional noise and reduces the state fidelity significantly. Nonetheless, ancilla-free ground state circuits could be implemented on chains of specific lengths like 12, 20, 28, etc., thanks to the presence of loops in the heavy-hexagonal lattice [54] with the corresponding numbers of transmons. With the scalable ansatz discussed in section VI, the closed-loop connectivity is not necessary and hence we discuss noisy simulations of Berry phase estimates from perturbed ground states for arbitrarily larger system sizes in Section VII B.

For  $n = 2$ , the ground state of the perturbed AKLT Hamiltonian under PBC can be expressed as follows:

$$|GS(\theta)\rangle = \alpha(\theta) |02\rangle + \beta(\theta) |11\rangle + \gamma(\theta) |20\rangle \quad (9)$$

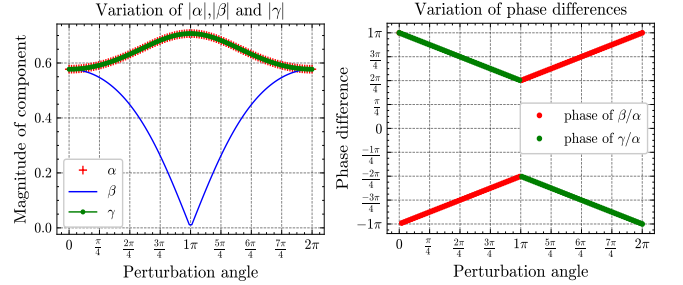


FIG. 6. **Variation of the magnitudes and phase differences of the components of the perturbed ground state vector.** The ground state vector  $\alpha(\theta)|02\rangle + \beta(\theta)|11\rangle + \gamma(\theta)|20\rangle$  variation is described in the figure. We note that  $|\alpha| = |\gamma|$  for all perturbation angles. At  $\theta = \pi$ , we observe that  $\beta = 0$ , coinciding with the point where the phase difference experiences a sudden discontinuity.

Without perturbation ( $\theta = 0$ ), the ground state vector is  $\frac{1}{\sqrt{3}} |02\rangle - \frac{1}{\sqrt{3}} |11\rangle + \frac{1}{\sqrt{3}} |20\rangle$  is maximally entangled. At  $\theta = \pi$ , the ground state vector is  $\frac{1}{\sqrt{2}} |02\rangle - \frac{1}{\sqrt{2}} |20\rangle$ . This state can be prepared with high fidelity using the same ansatz used for OBC states in Fig. 3. All other perturbations possess non-zero support on the three components  $|02\rangle$ ,  $|11\rangle$ , and  $|20\rangle$ . These states can be prepared to a high Hellinger fidelity (see Table II) using the ansatz circuit shown in Fig. 7. Details regarding the exact states, parameter optimisation for the ansatz in Fig. 7, and the hardware data corresponding to the

Table II can be found in the GitHub repository linked in Appendix E.

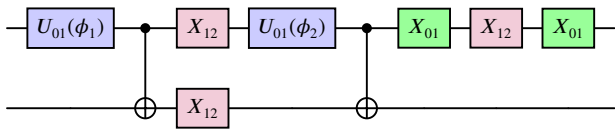


FIG. 7.  $n = 2$  PBC ansatz capturing the perturbed PBC ground states of  $n = 2$  AKLT for all perturbations. However, for  $\pi$ , ansatz with just a single entangling gate exists. The exact parameters used in these single qubit parameterised gates can be found in the Appendix E.

Perturbing angle	Hellinger fidelity%	Perturbing angle	Hellinger fidelity%
0	96.20%	$3\pi/2$	93.90%
$2\pi/3$	92.56%	$6\pi/5$	86.82%
$\pi/2$	88.87%	$6\pi/7$	86.66%
$2\pi/5$	90.17%	$10\pi/6$	94.28%
$2\pi/6$	92.72%	$8\pi/7$	92.31%
$2\pi/7$	93.91%	$10\pi/7$	94.05%
$4\pi/3$	88.94%	$8\pi/5$	90.48%
$4\pi/5$	92.55%	$12\pi/7$	90.40%
$4\pi/7$	94.84%	$\pi$	93.27%

TABLE II. Hellinger Fidelities of PBC  $n = 2$  states for various perturbation angles. The angles chosen here will be useful in computing the Berry phase in section VII A.

There are a few points to note regarding the ansatz circuit in Fig. 7. While the ansatz can be used to prepare a high Hellinger fidelity state, it is not guaranteed that phase differences between various components are captured accurately. This is because, in the second entangling gate of the ansatz, the control state is in general  $(0-1-2)$  manifold and this results in a non-negligible Stark phase shift amongst the vector components. Capturing these phases accurately is crucial for the berry phase as previously emphasized in Section IV. We discuss post selection (on the dominant components) based state tomography and phase correction to accurately capture the phase differences.

### A. Phase differences between the ground state vector components

Single qutrit gates produce ac-Stark shifts themselves in addition to the non-negligible Stark phase shift caused by the CNOT gate when the control qutrit is in  $|2\rangle$  state. This has been noted in [25, 26]. Empirically, the phase difference between the  $|02\rangle$  and  $|20\rangle$  components of the state produced by the real hardware circuit is  $\text{Arg}[\alpha/(\beta e^{i\phi_s})]$  where  $\phi_s$  is the contribution due to the Stark shift. We need to correct these additional  $\phi_s$  by performing a phase shift experiment by adding controllable phase differences to the state vector components. This experiment will be used to correct the unwanted phase accumulation from the Stark shift. Correcting

these phases has been explained in detail in Appendix 19. This method was previously implemented in [25] and works best for smaller systems like the one we will discuss. For general spin-1 systems, it is essential to construct a high-fidelity entangling gate like the one being studied in [53]. In the following section, we present noisy simulations of fidelities from scalable ansatz of the ground states which would be more suitable when the effect of noise sources such as charge dispersion, and ac-Stark shifts due to higher levels VA can be minimized in future devices.

## VI. SCALABLE STATE PREPARATION

In this section we describe a scalable method to prepare ground states of the PBC AKLT model with perturbation. We then use numerical simulations to show that qutrits lead to better state preparation than qubits in the presence of noise.

Note that AKLT ground states can be represented as matrix product states (MPS) of bond dimension two. This motivates the linear depth circuit ansatz [55] described in Fig. 8, where the repeated entangling operation  $V$  can be derived from the tensors of the MPS (see Eq. (3)). This operation can then be compiled onto the gate set available on either qutrit- or qubit-based hardware. Note that for the qubit-based compilation, we encode each bulk qutrit into a pair of qubits and use the following mapping of computational basis states:  $\{|0\rangle \rightarrow |00\rangle, |1\rangle \rightarrow |01\rangle, |2\rangle \rightarrow |10\rangle\}$ . More details regarding the compilation procedure can be found in Appendix G.

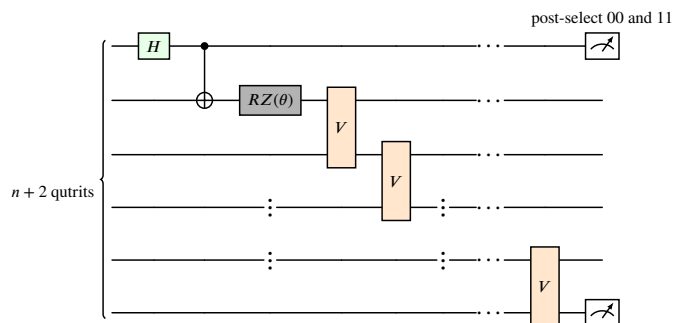


FIG. 8. **Scalable AKLT state preparation.** Ground state of PBC AKLT model with perturbation angle  $\theta$  is generated from an equal superposition of the 00 and 11 post-selected states. Note that for qubit-based implementation, each bulk qutrit must be encoded into two qubits. The  $H$  and  $RZ$  gates are standard qubit gates on a qubit device and the equivalent 0-1 manifold qutrit gates on a qutrit device. The entangling operation  $V$  can be derived from the tensors of the MPS representation of the ground state.

Note that the circuit described in Fig. 8 prepares the AKLT ground state by measuring the first and last qutrits and post-

selecting the outcomes:

$$|GS(\theta)\rangle = \frac{1}{\mathcal{N}_{00}} \langle 00|\psi(\theta)\rangle + \frac{1}{\mathcal{N}_{11}} \langle 11|\psi(\theta)\rangle, \quad (10)$$

where  $|\psi(\theta)\rangle$  is the pre-measurement state, and  $\mathcal{N}_{00}, \mathcal{N}_{11}$  ensure normalization. We numerically determine that the probabilities of outcomes 00 and 11 are approximately 0.25, irrespective of system size or perturbation angle. Therefore, this method for state preparation has only a small sampling overhead. This linear depth ansatz could be improved to constant depth circuits with the help of mid-circuit measurements and feed-forward operations at the cost of a constant factor in the qudits count as noted in [35, 56].

To illustrate the utility of qutrits, we simulate implementations of this state preparation method on qutrit- and qubit-based hardware in the presence of realistic noise. Our noise models (see Appendix H) take into account the thermalization of qubits and qutrits via the amplitude damping and dephasing channels, and can be simulated efficiently using tensor network techniques. We choose the two-norm fidelity (Appendix B) as the metric of success for state preparation.

Figure 9(a) shows that as we scale up system size, qutrits lead to preparations with significantly higher fidelity, both for noise rates available on existing devices and noise rates projected to be available on devices in the near future. This is because the compilation of the entangling operation,  $V$ , requires a larger number of CNOT gates on a qubit device.

Figure 9(b) highlights an important advantage of the state preparation scheme described above. The fidelity per site, defined as the  $n$ -th root of the two-norm fidelity for a system with  $n$  spins, remains stable across a range of system sizes when idling noise is suppressed via dynamical decoupling. This is because the ladder structure of the circuit allows only a constant amount of decoherence per site. Therefore, Fig. 8 provides a scalable method for studying ground state properties of the AKLT model.

## VII. BERRY PHASE

The topology of ground states of a spin-1 chain with time-reversal symmetry can be characterized by introducing a Berry phase for locally perturbed bonds [37, 57]. This differs from other methods for characterizing topological phases [58], which require extraction of the density matrix for a subsystem much larger than the correlation length of the system. Since Berry phase estimation is based on introducing a local perturbation, it is easier to implement on NISQ hardware.

We begin by defining the Berry phase in a quantum spin system. For a parameter-dependent Hamiltonian,  $H(\theta)$ , the Berry phase  $\gamma$  of the non-degenerate ground state is defined as

$$\gamma = -i \int_0^{2\pi} A(\theta) d\theta, \quad (11)$$

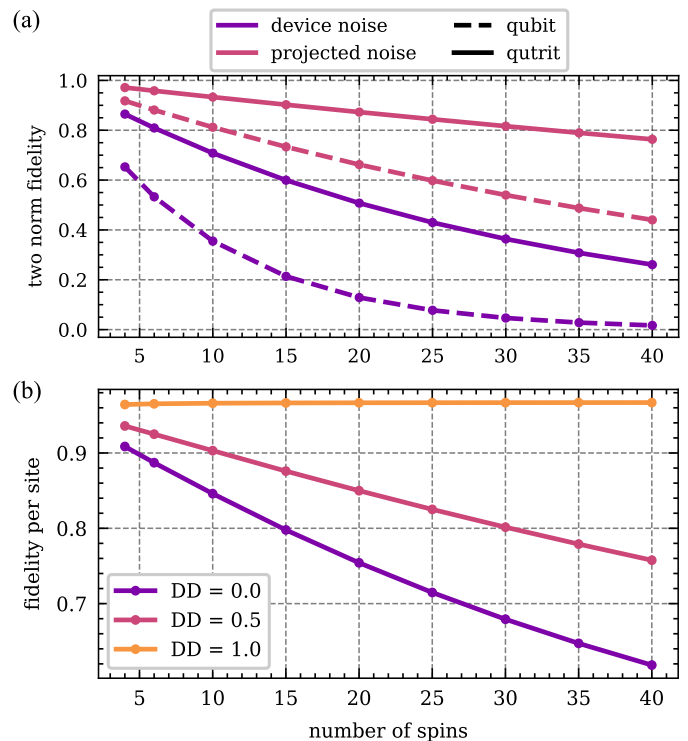


FIG. 9. **Simulation of state preparation in the presence of noise.** (a) Qutrit-based implementation consistently has higher fidelity than qubit-based implementation. The projected noise model uses  $T_1$  and  $T_2$  times that are five times longer than the ones measured on the physical device. (b) Effective dynamical decoupling (DD) leads to stable fidelity per site as we scale to large system sizes. DD of 0 and 1 correspond to no and perfect dynamical decoupling respectively.

where  $A(\theta)$  is the Abelian Berry connection obtained from the normalized ground state  $|GS(\theta)\rangle$  of  $H(\theta)$  as  $A(\theta) = \langle GS(\theta)|\partial_\theta|GS(\theta)\rangle$  and  $|GS(0)\rangle = |GS(2\pi)\rangle$ . We focus on non-degenerate ground states here. Refer to [59] for degenerate systems. We note that the Berry phase is real and quantized to 0 or  $\pi$  (mod  $2\pi$ ) if the Hamiltonian  $H(\theta)$  is invariant under any anti-unitary operation  $\Theta$ , *i.e.*  $[H(\theta), \Theta] = 0$ . The perturbation defined in Eq. (8) has time-reversal symmetry and, therefore, satisfies this condition. A Berry phase of  $\pi$  resulting from a perturbation on a bond between neighboring sites indicates the presence of a valence bond state, which has a non-trivial topology and entanglement.

To calculate the Berry phase numerically, we motivate a discrete approximation of it by partitioning the integration region in Eq. (11) with  $N - 1$  points between 0 to  $2\pi$

$$\begin{aligned} \langle GS(\theta)|\partial_\theta|GS(\theta)\rangle &\simeq \ln[1 + \delta\theta \langle GS(\theta)|\partial_\theta|GS(\theta)\rangle] \\ &\simeq \ln\langle GS(\theta)|GS(\theta + d\theta)\rangle = -i \text{Arg}\langle GS(\theta)|GS(\theta + d\theta)\rangle \end{aligned}$$

With this approximation, we can write a discretized expression for the Berry phase

$$\gamma_N = - \sum_{j=0}^{N-1} \text{Arg}\langle GS(\theta_j)|GS(\theta_{j+1})\rangle, \theta_j = \frac{2\pi}{N}j \quad (12)$$

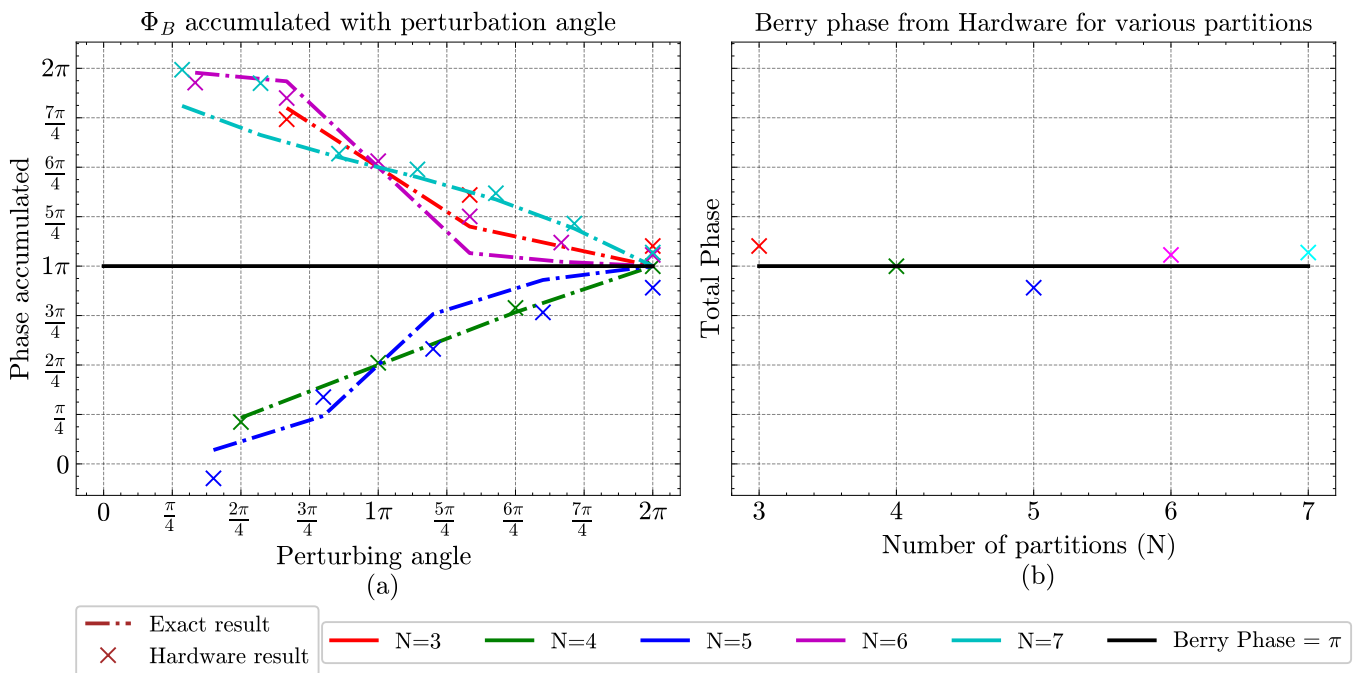


FIG. 10. **Berry phase from quantum hardware:** Panel (a) shows the accumulated phase when the ground state is perturbed as described in the main text (from perturbation angle 0 to  $2\pi$ ) for various numbers of partitions. A common gauge vector is picked so that the partial sums in the Eq. (12) from the quantum hardware plotted with  $\times$ 's can be compared against the noiseless classical results plotted as dashed lines. Panel (b) represents the final values of Berry phase for various number of partitions.

It is important to note that the Berry phase is independent of any global phase associated with the perturbed ground states  $|GS(\theta)\rangle$ . However, to compare the accuracy of the partial sums in the Berry phase computation with classical methods such as exact diagonalization or density matrix renormalization group, it is essential to compute the phases using the same gauge for all methods. This is called gauge fixing and is done by picking a random gauge vector  $|g\rangle$  and replacing  $|GS(\theta)\rangle$  with  $\langle GS(\theta)|g\rangle|GS(\theta)\rangle$ . This procedure fixes any global phase difference between the states produced by classical and quantum methods and allows us to compare their partial sums and not just the (previously) gauge invariant  $\gamma_N$ .

#### A. Berry phase from quantum hardware

In this section, we compute the Berry phase for the  $n = 2$  PBC AKLT chain from data collected on quantum hardware.

Note that at zero perturbation, a slight modification to the coefficient of the quartic term is necessary to break the degeneracy of the ground states and avoid ambiguity when computing Eq. (11). We modify the coefficient from  $\frac{1}{3}$  to  $\frac{1}{3} - \epsilon$ , where  $\epsilon$  is a small positive number.

The circuit in Fig. 7 can be used to prepare, with high Hellinger fidelity, the states required to compute the Berry

phase defined in Eq. (12). The relevant phase differences between the dominant components in the vector can be corrected and measured to high accuracy using state tomography. (see Appendix F, specifically Fig. 18 and Fig. 22). Phases attached to non-dominant components are noisy and, due to their small magnitudes, their contribution to the overall Berry phase is negligible. Alternatively, one could post-select the dominant components and obtain the overall Berry phase from them.

Statevectors corresponding to the perturbing angles shown in Table II are sufficient to compute Eq. (12) with 3, 4, 5, 6 and 7 partitions of the  $[0, 2\pi]$  interval. Fig. 10 presents the results of our experiment. The final Berry phases obtained match the expected value of  $\pi$  up to an error of roughly 10% for various choices of partitions. The observed accuracy in the Berry phase and the partial sums (after gauge fixing) can be attributed to the high fidelity of state preparation (Table II). The convergence of the Berry phase to  $\pi$  for more than three partitions can be confirmed through classical simulation. To compute Berry phase of general spin-1 systems, one must first run an analysis on the required number of partitions to observe convergence to the expected value. The hardware data and runs corresponding to Fig. 10 can be found in the GitHub repository linked in Appendix E.

Computing individual phase differences (and eventually the Berry phase) for larger system sizes using this method will be expensive, although classical shadows [60] provide a possible



means of reducing the number of circuits required. However, a more straightforward approach is to use a modified Hadamard test alongside the state preparation scheme we described in section VI. We explore this possibility next.

### B. Scalable computation of Berry phase

We now discuss a scalable method to compute Berry phase of the AKLT model and then benchmark this method with numerical simulations in the presence of noise.

The Hadamard test is a standard tool for computing overlaps of quantum states. Unlike related methods like the swap test, it allows one to extract the complex value of the overlap. Therefore, it is ideal for computing  $\text{Arg}\langle GS(\theta_j)|GS(\theta_{j+1})\rangle$  in Eq. (12). The Hadamard test requires as input circuits that prepare  $|GS(\theta_j)\rangle$ . We propose using the circuit in Fig. 8. However, the post-selection step therein is incompatible with the standard Hadamard test since it requires performing a conditional measurement and reset, which is an unphysical operation. Therefore, we construct a modified Hadamard test that can work with post-selection based state preparation schemes. This algorithm is described in detail in Appendix I.

Figure 11(a) shows a simulation of our algorithm in the presence of noise. While the circuit depth required to implement this algorithm scales well with system size, it is still beyond the reach of existing hardware. Therefore, the noise model in our simulation uses coherence times that are 25 times longer than the ones measured on the device. We observe that in this regime the Berry phase can be computed accurately for systems of upto 20 spins, after which the algorithm fails as a result of noise.

Figure 11(b) simulates Berry phase computation for a system of 4 spins as the noise rate is varied. The noise rate is defined as the ratio between the actual coherence times measured on the device and the longer coherence times used in our simulation. We observe that the Berry phase remains robust for a range of noise rates before abruptly decaying to zero. We interpret this as a phase transition in the learnability of topological properties as a function of noise. This observed phenomenon might be of independent scientific interest as a new setting for studying learnability transitions [61].

## VIII. CONCLUSION

In this work, we explored transmon qutrit-based encoding schemes to prepare ground-state circuits of the well-studied spin-1 AKLT Hamiltonian. The approaches discussed here are applicable beyond the specific spin-1 system, provided the ground states are not highly entangled and have simple qutrit circuit representations, similar to the qubit-based problems. In a noise-free setup, we always expect improvements in qutrit encoding over qubit-based encoding for spin-1 systems. However, accessing higher transmon levels introduces

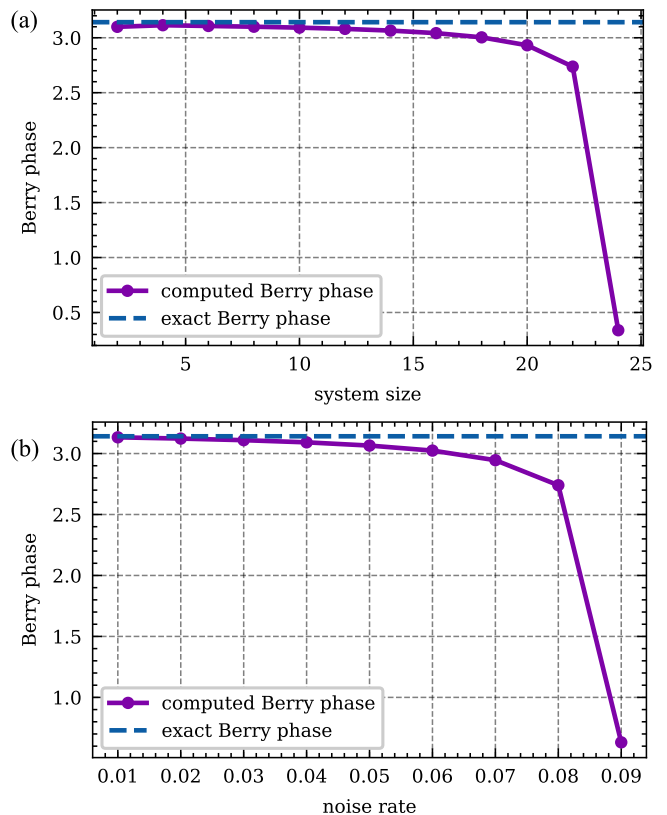


FIG. 11. **Simulation of Berry phase computation in the presence of noise** (a) across system sizes and (b) across noise rates. The Berry phase remains close to the expected value of  $\pi$  for a range of system sizes and noise rates, before sharply decaying to zero. We identify this as a phase transition in the learnability of topological properties of the AKLT state. For panel (a) the noise rate was fixed at 0.04 and for panel (b) the system consisted of 10 spins. All Berry phases were computed using 4 partitions of the  $[0, 2\pi]$  interval of perturbing angles.

additional noise sources, which may negate any noise-free improvements for certain problems. Therefore, one should carefully assess when qutrit-based simulations offer an advantage over conventional qubit-based schemes.

Most of the shortcomings discussed in the manuscript are due to the absence of high-fidelity entangling qutrit gates. With recent efforts in creating such gates [53], the effect of noise from higher levels might play a less significant role as our noisy simulations demonstrate. Regardless, a takeaway from this work is that, by consciously coming up with qutrit-based circuits to minimize the noise due to higher levels, one can tap into the full potential of qutrit-based encoding schemes. This was demonstrated through high-fidelity state ground state preparations and Berry phase estimation from hardware. These results were extended to larger system sizes using tensor network based simulation in the presence of noise.

The methods discussed in this work might be applicable to various spin-1 physics simulations in high energy physics [62–

[64], statistical physics [65–67] and cosmology [68]. Another interesting direction is the study of time evolution of spin-1 systems. Qubit-encoding of such problems requires a modification to conventional Trotter approaches [18]. The methods described in this work could open up new avenues for the study of the dynamics of spin-1 systems. This constitutes a potential future step of our work.

## IX. ACKNOWLEDGMENTS

We would like to acknowledge the funding from the Office of Science through the Quantum Science Center (QSC), a Na-

tional Quantum Information Science Research Center. We acknowledge the use of IBM Quantum services for this work. L.C. was partially supported by Laboratory Directed Research and Development program of Los Alamos National Laboratory under project number 20230049DR. A.B. acknowledges Paul Kairys for insightful discussions related to this work. This research used resources of the Oak Ridge Leadership Computing Facility, which is a DOE Office of Science User Facility supported under Contract DE-AC05-00OR22725.

- 
- [1] J. Preskill, Quantum Computing in the NISQ era and beyond, *Quantum* **2**, 79 (2018).
- [2] Y. Kim, A. Eddins, S. Anand, K. X. Wei, E. van den Berg, S. Rosenblatt, H. Nayfeh, Y. Wu, M. Zaletel, K. Temme, and A. Kandala, Evidence for the utility of quantum computing before fault tolerance, *Nature* **618**, 500 (2023).
- [3] D. Alevras, M. Metkar, T. Yamamoto, V. Kumar, T. Friedhoff, J.-E. Park, M. Takeori, M. LaDue, W. Davis, and A. Galda, mRNA secondary structure prediction using utility-scale quantum computers (2024), arXiv:2405.20328 [quant-ph].
- [4] J. Robledo-Moreno, M. Motta, H. Haas, A. Javadi-Abhari, P. Jurcevic, W. Kirby, S. Martiel, K. Sharma, S. Sharma, T. Shirakawa, I. Sitdikov, R.-Y. Sun, K. J. Sung, M. Takita, M. C. Tran, S. Yunoki, and A. Mezzacapo, Chemistry Beyond Exact Solutions on a Quantum-Centric Supercomputer (2024), arXiv:2405.05068 [quant-ph].
- [5] K. Shinjo, K. Seki, T. Shirakawa, R.-Y. Sun, and S. Yunoki, Unveiling clean two-dimensional discrete time quasicrystals on a digital quantum computer (2024), arXiv:2403.16718 [quant-ph].
- [6] R. C. Farrell, M. Illa, A. N. Ciavarella, and M. J. Savage, Quantum Simulations of Hadron Dynamics in the Schwinger Model using 112 Qubits (2024), arXiv:2401.08044 [quant-ph].
- [7] I. Affleck, Quantum spin chains and the Haldane gap, *Journal of Physics: Condensed Matter* **1**, 3047 (1989).
- [8] J. Ren, W.-L. You, and A. M. Ole's, Quantum phase transitions in a spin-1 antiferromagnetic chain with long-range interactions and modulated single-ion anisotropy, *Physical Review B* (2020).
- [9] D. Jacob, L. Shao, V. Corre, T. Zibold, L. De Sarlo, E. Mimoun, J. Dalibard, and F. Gerbier, Phase diagram of spin-1 antiferromagnetic Bose-Einstein condensates, *Phys. Rev. A* **86**, 061601 (2012).
- [10] G. Catarina and J. Fernández-Rossier, Hubbard model for spin-1 Haldane chains, *Phys. Rev. B* **105**, L081116 (2022).
- [11] R. Majumdar, S. Basu, S. Ghosh, and S. Sur-Kolay, Quantum error-correcting code for ternary logic, *Phys. Rev. A* **97**, 052302 (2018).
- [12] S. Muralidharan, C.-L. Zou, L. Li, J. Wen, and L. Jiang, Overcoming erasure errors with multilevel systems, *New Journal of Physics* **19**, 013026 (2017).
- [13] Security of quantum key distribution with entangled qutrits, author = Durt, Thomas and Cerf, Nicolas J. and Gisin, Nicolas and Żukowski, Marek, *Phys. Rev. A* **67**, 012311 (2003).
- [14] S. P. Walborn, D. S. Lemelle, M. P. Almeida, and P. H. S. Ribeiro, Quantum Key Distribution with Higher-Order Alphabets Using Spatially Encoded Qudits, *Phys. Rev. Lett.* **96**, 090501 (2006).
- [15] A. Bocharov, M. Roetteler, and K. M. Svore, Factoring with qutrits: Shor's algorithm on ternary and metaplectic quantum architectures, *Phys. Rev. A* **96**, 012306 (2017).
- [16] Asymptotically Optimal Quantum Circuits for  $d$ -Level Systems, author = Bullock, Stephen S. and O'Leary, Dianne P. and Brennen, Gavin K., *Phys. Rev. Lett.* **94**, 230502 (2005).
- [17] A. Pavlidis and E. Floratos, Quantum-Fourier-transform-based quantum arithmetic with qudits, *Phys. Rev. A* **103**, 032417 (2021).
- [18] O. Ogunkoya, J. Kim, B. Peng, A. B. i. e. i. f. m. c. Özgüler, and Y. Alexeev, Qutrit circuits and algebraic relations: A pathway to efficient spin-1 Hamiltonian simulation, *Phys. Rev. A* **109**, 012426 (2024).
- [19] M. S. Blok, V. V. Ramasesh, T. Schuster, K. O'Brien, J. M. Kreikebaum, D. Dahlen, A. Morvan, B. Yoshida, N. Y. Yao, and I. Siddiqi, Quantum Information Scrambling on a Superconducting Qutrit Processor, *Phys. Rev. X* **11**, 021010 (2021).
- [20] Universal Qudit Gate Synthesis for Transmons, author = Fischer, Laurin E. and Chiesa, Alessandro and Tacchino, Francesco and Egger, Daniel J. and Carretta, Stefano and Tavernelli, Ivano, *PRX Quantum* **4**, 030327 (2023).
- [21] N. Goss, A. Morvan, B. Marinelli, B. K. Mitchell, L. B. Nguyen, R. K. Naik, L. Chen, C. Jünger, J. M. Kreikebaum, D. I. Santiago, J. J. Wallman, and I. Siddiqi, High-fidelity qutrit entangling gates for superconducting circuits, *Nature Communications* **13**, 7481 (2022).
- [22] Y. Chi, J. Huang, Z. Zhang, J. Mao, Z. Zhou, X. Chen, C. Zhai, J. Bao, T. Dai, H. Yuan, M. Zhang, D. Dai, B. Tang, Y. Yang, Z. Li, Y. Ding, L. K. Oxenløwe, M. G. Thompson, J. L. O'Brien, Y. Li, Q. Gong, and J. Wang, A programmable qudit-based quantum processor, *Nature Communications* **13**, 1166 (2022).
- [23] P. Hrmo, B. Wilhelm, L. Gerster, M. W. van Mourik, M. Huber, R. Blatt, P. Schindler, T. Monz, and M. Ringbauer, Native qudit entanglement in a trapped ion quantum processor, *Nature Communications* **14**, 2242 (2023).
- [24] M. Ringbauer, M. Meth, L. Postler, R. Stricker, R. Blatt, P. Schindler, and T. Monz, A universal qudit quantum processor with trapped ions, *Nature Physics* **18**, 1053 (2022).
- [25] A. Galda, M. Cubeddu, N. Kanazawa, P. Narang, and N. Earnest-Noble, Implementing a Ternary Decomposition of the Toffoli Gate on Fixed-Frequency Transmon Qutrits (2021),

- arXiv:2109.00558 [quant-ph].
- [26] A. Cervera-Lierta, M. Krenn, A. Aspuru-Guzik, and A. Galda, Experimental High-Dimensional Greenberger-Horne-Zeilinger Entanglement with Superconducting Transmon Qutrits, *Phys. Rev. Appl.* **17**, 024062 (2022).
- [27] D. Willsch, D. Rieger, P. Winkel, M. Willsch, C. Dickel, J. Krause, Y. Ando, R. Lescanne, Z. Leghtas, N. T. Bronn, P. Deb, O. Lanes, Z. K. Mineev, B. Dennig, S. Geisert, S. Günzler, S. Ihssen, P. Paluch, T. Reisinger, R. Hanna, J. H. Bae, P. Schüffelgen, D. Grützmacher, L. Buimaga-Iarinca, C. Morari, W. Wernsdorfer, D. P. DiVincenzo, K. Michielsen, G. Catelani, and I. M. Pop, Observation of Josephson harmonics in tunnel junctions, *Nature Physics* **20**, 815–821 (2024).
- [28] I. Affleck, T. Kennedy, E. H. Lieb, and H. Tasaki, Rigorous results on valence-bond ground states in antiferromagnets, *Phys. Rev. Lett.* **59**, 799 (1987).
- [29] C. L. Kane and E. J. Mele, Quantum Spin Hall Effect in Graphene, *Phys. Rev. Lett.* **95**, 226801 (2005).
- [30] J. E. Moore and L. Balents, Topological invariants of time-reversal-invariant band structures, *Phys. Rev. B* **75**, 121306 (2007).
- [31] R. Roy, Topological phases and the quantum spin Hall effect in three dimensions, *Phys. Rev. B* **79**, 195322 (2009).
- [32] M. den Nijs and K. Rommelse, Preroughening transitions in crystal surfaces and valence-bond phases in quantum spin chains, *Phys. Rev. B* **40**, 4709 (1989).
- [33] T.-C. Wei, I. Affleck, and R. Raussendorf, Affleck-Kennedy-Lieb-Tasaki State on a Honeycomb Lattice is a Universal Quantum Computational Resource, *Phys. Rev. Lett.* **106**, 070501 (2011).
- [34] T. Chen, R. Shen, C. H. Lee, and B. Yang, High-fidelity realization of the AKLT state on a NISQ-era quantum processor, *SciPost Physics* **15**, 10.21468/scipostphys.15.4.170 (2023).
- [35] Smith, Kevin and Crane, Eleanor and Wiebe, Nathan and Girvin, S.M., Deterministic constant-depth preparation of the aklt state on a quantum processor using fusion measurements, *PRX Quantum* **4** (2023).
- [36] C. L. Edmunds, E. Rico, I. Arrazola, G. K. Brennen, M. Meth, R. Blatt, and M. Ringbauer, *Constructing the spin-1 Haldane phase on a qudit quantum processor* (2024), arXiv:2408.04702 [quant-ph].
- [37] T. Hirano, H. Katsura, and Y. Hatsugai, Topological classification of gapped spin chains: Quantized Berry phase as a local order parameter, *Physical Review B* **77**, 10.1103/physrevb.77.094431 (2008).
- [38] T. Hirano, H. Katsura, and Y. Hatsugai, Topological classification of gapped spin chains: Quantized Berry phase as a local order parameter, *Physical Review B* **77**, 10.1103/physrevb.77.094431 (2008).
- [39] J. Richert, The Berry phase: A topological test for the spectrum structure of frustrated quantum spin systems, *Physics Letters A* **372**, 5352 (2008).
- [40] K. S. Novoselov, E. McCann, S. V. Morozov, V. I. Fal'ko, M. I. Katsnelson, U. Zeitler, D. Jiang, F. Schedin, and A. K. Geim, Unconventional quantum Hall effect and Berry's phase of  $2\pi$  in bilayer graphene, *Nature Physics* **2**, 177 (2006).
- [41] K. Hida, Crossover between the Haldane-gap phase and the dimer phase in the spin-1/2 alternating Heisenberg chain, *Phys. Rev. B* **45**, 2207 (1992).
- [42] F. D. M. Haldane, Nonlinear Field Theory of Large-Spin Heisenberg Antiferromagnets: Semiclassically Quantized Solitons of the One-Dimensional Easy-Axis Néel State, *Phys. Rev. Lett.* **50**, 1153 (1983).
- [43] M. Oshikawa, Hidden  $Z_2 \times Z_2$  symmetry in quantum spin chains with arbitrary integer spin, *Journal of Physics: Condensed Matter* **4**, 7469 (1992).
- [44] R. D. East, J. van de Wetering, N. Chancellor, and A. G. Grushin, AKLT-States as ZX-Diagrams: Diagrammatic Reasoning for Quantum States, *PRX Quantum* **3**, 010302 (2022).
- [45] D. C. McKay, C. J. Wood, S. Sheldon, J. M. Chow, and J. M. Gambetta, Efficient Z gates for quantum computing, *Phys. Rev. A* **96**, 022330 (2017).
- [46] T. Alexander, N. Kanazawa, D. J. Egger, L. Capelluto, C. J. Wood, A. Javadi-Abhari, and D. C McKay, Qiskit pulse: programming quantum computers through the cloud with pulses, *Quantum Science and Technology* **5**, 044006 (2020).
- [47] S. Sheldon, L. S. Bishop, E. Magesan, S. Filipp, J. M. Chow, and J. M. Gambetta, Characterizing errors on qubit operations via iterative randomized benchmarking, *Physical Review A* **93**, 012301 (2016).
- [48] F. Motzoi, J. M. Gambetta, P. Rebentrost, and F. K. Wilhelm, Simple Pulses for Elimination of Leakage in Weakly Nonlinear Qubits, *Physical Review Letters* **103**, 110501 (2009).
- [49] Demonstration of quantum volume 64 on a superconducting quantum computing system, *Quantum Science and Technology* **6**, 10.1088/2058-9565/abe519 (2021).
- [50] E. Magesan, J. M. Gambetta, and J. Emerson, Scalable and Robust Randomized Benchmarking of Quantum Processes, *Physical Review Letters* **106**, 180504 (2011).
- [51] E. Magesan, J. M. Gambetta, A. D. Córcoles, and J. M. Chow, Machine Learning for Discriminating Quantum Measurement Trajectories and Improving Readout, *Phys. Rev. Lett.* **114**, 200501 (2015).
- [52] S. Rosenblum, P. Reinhold, M. Mirrahimi, L. Jiang, L. Frunzio, and R. J. Schoelkopf, Fault-tolerant detection of a quantum error, *Science* **361**, 266–270 (2018).
- [53] N. Goss, A. Morvan, B. Marinelli, B. K. Mitchell, L. B. Nguyen, R. K. Naik, L. Chen, C. Jünger, J. M. Kreikebaum, D. I. Santiago, J. J. Wallman, and I. Siddiqi, High-fidelity qutrit entangling gates for superconducting circuits, *Nature Communications* **13**, 10.1038/s41467-022-34851-z (2022).
- [54] Topological and subsystem codes on low-degree graphs with flag qubits, *Physical Review X* **10**, 1 (2019).
- [55] S.-J. Ran, Encoding of matrix product states into quantum circuits of one- and two-qubit gates, *Physical Review A* **101**, 10.1103/physreva.101.032310 (2020).
- [56] K. C. Smith, A. Khan, B. K. Clark, S. Girvin, and T.-C. Wei, Constant-Depth Preparation of Matrix Product States with Adaptive Quantum Circuits, *PRX Quantum* **5**, 030344 (2024).
- [57] Y. Hatsugai, Quantized Berry phases for a local characterization of spin liquids in frustrated spin systems, *Journal of Physics: Condensed Matter* **19**, 145209 (2007).
- [58] F. Pollmann and A. M. Turner, Detection of symmetry-protected topological phases in one dimension, *Physical Review B* **86**, 10.1103/physrevb.86.125441 (2012).
- [59] Y. Hatsugai, Explicit Gauge Fixing for Degenerate Multiplets: A Generic Setup for Topological Orders, *Journal of the Physical Society of Japan* **73**, 2604–2607 (2004).
- [60] H.-Y. Huang, R. Kueng, and J. Preskill, Predicting many properties of a quantum system from very few measurements, *Nature Physics* **16**, 1050–1057 (2020).
- [61] M. Ippoliti and V. Khemani, Learnability Transitions in Monitored Quantum Dynamics via Eavesdropper's Classical Shadows, *PRX Quantum* **5**, 10.1103/prxquantum.5.020304 (2024).
- [62] P. W. Higgs, Broken Symmetries and the Masses of Gauge Bosons, *Phys. Rev. Lett.* **13**, 508 (1964).

- [63] S. Weinberg, Non-Abelian Gauge Theories of the Strong Interactions, *Phys. Rev. Lett.* **31**, 494 (1973).
- [64] M. Gell-Mann, Symmetries of Baryons and Mesons, *Phys. Rev.* **125**, 1067 (1962).
- [65] M. Blume, Theory of the First-Order Magnetic Phase Change in  $\text{UO}_2$ , *Phys. Rev.* **141**, 517 (1966).
- [66] F. Y. Wu, The Potts model, *Rev. Mod. Phys.* **54**, 235 (1982).
- [67] M. Sajjan, H. Alaeian, and S. Kais, Magnetic phases of spatially modulated spin-1 chains in Rydberg excitons: Classical and quantum simulations, *The Journal of Chemical Physics* **157**, 224111 (2022), [https://pubs.aip.org/aip/jcp/article-pdf/doi/10.1063/5.0128283/16555379/224111\\_1\\_online.pdf](https://pubs.aip.org/aip/jcp/article-pdf/doi/10.1063/5.0128283/16555379/224111_1_online.pdf).
- [68] A. Golovnev, V. Mukhanov, and V. Vanchurin, Vector inflation, *Journal of Cosmology and Astroparticle Physics* **2008** (06), 009.
- [69] various authors, *Qiskit Textbook* (Github, 2023).
- [70] R. T. Thew, K. Nemoto, A. G. White, and W. J. Munro, Qudit quantum-state tomography, *Physical Review A* **66**, 10.1103/physreva.66.012303 (2002).
- [71] S. Cao, D. Lall, M. Bakr, G. Campanaro, S. Fasciati, J. Wills, V. Chidambaram, B. Shteynas, I. Rungger, and P. Leek, Efficient qutrit gate-set tomography on a transmon (2022), [arXiv:2210.04857 \[quant-ph\]](https://arxiv.org/abs/2210.04857).
- [72] G. Evenbly and G. Vidal, Algorithms for Entanglement Renormalization: Boundaries, Impurities and Interfaces, *Journal of Statistical Physics* **157**, 931–978 (2014).
-

### Appendix A: Matrix representations of qutrit gates

Matrix representations of single qutrit gates used in the ground state circuits compilation.

$$X_{01} = \begin{bmatrix} 0 & -i & 0 \\ -i & 0 & 0 \\ 0 & 0 & 1 \end{bmatrix}, \quad X_{12} = \begin{bmatrix} 1 & 0 & 0 \\ 0 & 0 & -i \\ 0 & -i & 0 \end{bmatrix} \quad (\text{A1})$$

$$\sqrt{X_{01}} = \begin{bmatrix} \frac{1}{\sqrt{2}} & \frac{-i}{\sqrt{2}} & 0 \\ \frac{-i}{\sqrt{2}} & \frac{1}{\sqrt{2}} & 0 \\ 0 & 0 & 1 \end{bmatrix}, \quad \sqrt{X_{12}} = \begin{bmatrix} 1 & 0 & 0 \\ 0 & \frac{1}{\sqrt{2}} & \frac{-i}{\sqrt{2}} \\ 0 & \frac{-i}{\sqrt{2}} & \frac{1}{\sqrt{2}} \end{bmatrix} \quad (\text{A2})$$

$$RZ_{01}(\phi) = \begin{bmatrix} 1 & 0 & 0 \\ 0 & e^{i\phi} & 0 \\ 0 & 0 & 1 \end{bmatrix}, \quad RZ_{12}(\phi) = \begin{bmatrix} 1 & 0 & 0 \\ 0 & 1 & 0 \\ 0 & 0 & e^{i\phi} \end{bmatrix} \quad (\text{A3})$$

The truth table of CNOT gate used in the ground state preparation circuits compilation (Followed from [26])

Control	Target	Output
$ 0\rangle$	$ 0\rangle$	$ 00\rangle$
$ 0\rangle$	$ 1\rangle$	$ 01\rangle$
$ 0\rangle$	$ 2\rangle$	$ 02\rangle$
$ 1\rangle$	$ 0\rangle$	$ 10\rangle$
$ 1\rangle$	$ 1\rangle$	$ 11\rangle$
$ 1\rangle$	$ 2\rangle$	$i 12\rangle$
$ 2\rangle$	$ 0\rangle$	$a 20\rangle + b 21\rangle$
$ 2\rangle$	$ 1\rangle$	$b^* 20\rangle + c 21\rangle$
$ 2\rangle$	$ 2\rangle$	$e^{i\delta} 22\rangle$

TABLE III. Truth table of default IBM CNOT gate

Some parts of our circuits involve the application of  $U$  gate on the qutrits completely in the  $0-1$  manifold. We call such gates as  $U_{01}$  gate and their matrix representation is as follows

$$U_{01}(\theta, \phi, \lambda) = \begin{bmatrix} \cos(\theta/2) & -e^{i\lambda} \sin(\theta/2) \\ e^{i\phi} \sin(\theta/2) & e^{i(\phi+\lambda)} \cos(\theta/2) \end{bmatrix} \quad (\text{A4})$$

The values of  $a$ ,  $b$ ,  $c$  and  $\delta$  vary based on the device and the qutrit pairs of interest. For the purpose of noisy simulations performed in this work, we chose  $a = 1/\sqrt{2}$ ,  $b = -1/\sqrt{2}$ ,  $c = -1/\sqrt{2}$  and  $\delta = -\pi/2$ .

### Appendix B: Fidelity definitions

**Hellinger fidelity** of two probability distributions/vectors  $\mathcal{Q}_1 = (\mathcal{Q}_1(1), \mathcal{Q}_1(2), \dots, \mathcal{Q}_1(n))$  and  $\mathcal{Q}_2 = (\mathcal{Q}_2(1), \mathcal{Q}_2(2), \dots, \mathcal{Q}_2(n))$  with  $n$  elements each is given by

$$H = \left( \sum_{i=1}^n \sqrt{\mathcal{Q}_1(i) \times \mathcal{Q}_2(i)} \right)^2 \quad (\text{B1})$$

**Quantum fidelity** between states  $\rho$  and  $\sigma$  is defined as

$$F(\rho, \sigma) = \left( \text{tr} \sqrt{\sqrt{\rho} \sigma \sqrt{\rho}} \right)^2. \quad (\text{B2})$$

Quantum fidelity can be interpreted as a distance measure on probability distributions represented by density matrices. It also generalizes the notion of overlaps to mixed states. However, it is intractable to compute for states of many particles, even when the states have efficient tensor network representations. This is because the square root in the definition requires all the eigenvalues of the exponentially large density matrices.

**Two-norm fidelity** is defined using the Schatten 2-norm,  $\|\cdot\|_2$ , on the vector space of operators:

$$F_2(\rho, \sigma) = \frac{1}{2} \left( \text{tr}(\rho^2) + \text{tr}(\sigma^2) - \|\rho - \sigma\|_2 \right) = \text{tr}(\rho\sigma) \quad (\text{B3})$$

While two-norm fidelity does not have an interpretation as a statistical distance, it is easy to compute for density matrices represented as matrix product operators of low bond dimension. In fact, it can be expressed as a standard contraction of two matrix product operators.

We further justify the use of two-norm fidelity as a metric of success in our numerical simulations by showing that it approximates the quantum fidelity in the low-noise regime. Suppose  $\rho$  and  $\sigma$  are almost pure states, in the sense that they each have diagonalizations of the form:

$$\rho = (1 - \epsilon) |\psi_1\rangle \langle \psi_1| + \frac{\epsilon}{N-1} \sum_{j=2}^N |\psi_j\rangle \langle \psi_j| \quad (\text{B4})$$

$$\sigma = (1 - \epsilon) |\phi_1\rangle \langle \phi_1| + \frac{\epsilon}{N-1} \sum_{j=2}^N |\phi_j\rangle \langle \phi_j|, \quad (\text{B5})$$

for small  $\epsilon$ . Note that the density matrices do not have to commute and the bases in which they are diagonal can be different. The purity of each matrix is approximately  $(1 - \epsilon)^2$ :

$$\text{tr}(\rho^2) = \text{tr}(\sigma^2) = (1 - \epsilon)^2 + \mathcal{O}\left(\frac{\epsilon^2}{N}\right). \quad (\text{B6})$$

We can now expand quantum fidelity and two-norm fidelity in powers of  $\epsilon$ :

$$F(\rho, \sigma) = (1 - \epsilon)^2 |\langle \psi | \phi \rangle|^2 + \mathcal{O}\left(\frac{\sqrt{\epsilon}}{N-1}\right) \quad (\text{B7})$$

$$F_2(\rho, \sigma) = (1 - \epsilon)^2 |\langle \psi | \phi \rangle|^2 + \mathcal{O}\left(\frac{\epsilon}{N-1}\right) \quad (\text{B8})$$

We observe that the two expressions are equal to order  $\sqrt{\epsilon}$ . In the low-noise regime, states have purities close to 1 and, therefore, the two-norm fidelity is a good approximation for quantum fidelity.

### Appendix C: Device specifications

Qubit #:	Qubit 1	Qubit 2	Qubit 3	Qubit 4
Frequency (GHz)	5.155	5.256	5.097	5.0728
Anharmonicity(GHz)	-0.3421	-0.3396	-0.3427	-0.3429
$T_1(\mu s)$	146.485	173.626	140.629	163.587
$T_2(\mu s)$	145.647	221.524	28.345	14.850
Readout assignment error	0.0109	0.0177	0.009	0.0086

TABLE IV. **Calibration details of *ibm\_hanoi***: Listed in this table are some of the calibration details of *ibm\_hanoi* when using it to prepare high-fidelity AKLT ground states. For  $n = 2$  (both OBC and PBC (Fig. 3, Fig. 7)), qubits 1 and 2 were used. For  $n = 3$  (Fig. 4), qubits 1, 2 and 3 were used. For  $n = 4$  (Fig. 5), qubits 1, 2, 3 and 4 were used. Qubits 3, 2, 1 and 4 exist in a single linear chain in that order.

### Appendix D: Calibration details

To achieve a high-fidelity  $X_{12}$  gate, we start with narrow-band spectroscopy to get a rough estimate of the  $1-2$  frequency. This is followed by a more detailed calibration procedure at around this frequency as described below. The following experiments are performed sandwiched between two  $X_{01}$  so that they occur in the  $1-2$  manifold of the qutrit.

#### 1. Rough Rabi experiment

A Gaussian pulse of the same duration as a single qubit gate is applied at the estimated  $1-2$  frequency by varying the amplitude of the drive as shown in Fig. 12(a). The amplitude at which the signal reaches the maximum population of  $|2\rangle$  gives us a rough estimate of the amplitude required for the  $X_{12}$  pulse.

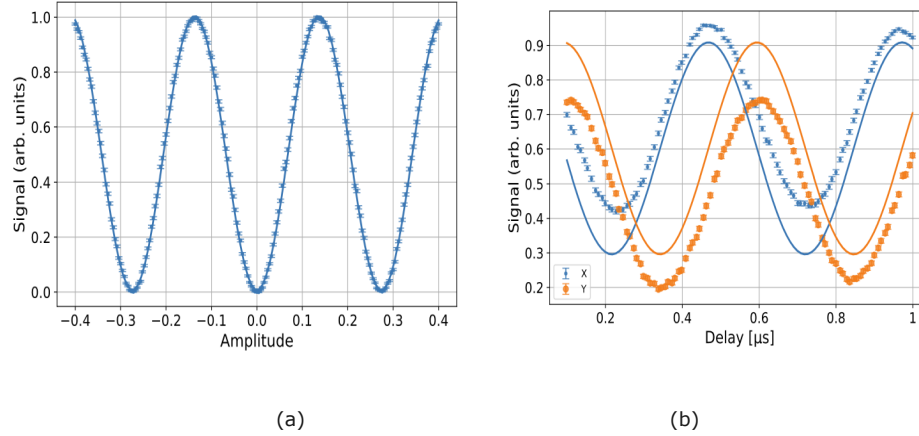


FIG. 12. Rough Rabi (a) and Rough Ramsey (b) experiments on the  $1-2$  manifold. The plot here shows a run on the qubit 4 of the *ibm\_auckland* device. These experiments are followed by fine Rabi and fine Ramsey experiments to fine-tune the amplitude and frequency required for the  $X_{12}$  drive pulse. The Ramsey experiments are offset due to the presence of charge dispersion in the  $1-2$  transition frequency [27].

#### 2. Rough Ramsey Experiment

The rough amplitude obtained in the rough Rabi experiment is used to perform the rough Ramsey experiment. Here, we sweep the delay between two  $\pi/2$  pulses applied at the roughly estimated  $1-2$  frequency such that the phase of the second pulse gets changed by introducing delays between the pulses to fine-tune the calibration of the qutrit  $1-2$  frequency (Fig. 12). The frequency of fringes observed in the experiment gives us an estimate of the frequency offset from the original  $1-2$  frequency.

### 3. Fine Experiments

Following the calibration the amplitude of the truncated Gaussian envelope and frequency  $f_{12}$  of the pulse carrier that implements the  $X_{12}$  and  $\sqrt{X_{12}}$  gates, these are further refined by error-amplified versions of the Rabi and Ramsey experiments [47]. Then a derivative removal by an adiabatic gate (DRAG) correction [48] is applied to the quadrature component, the amplitude of which is determined by error-amplified rotary ( $\sqrt{X_{12}} - \sqrt{X_{12}^\dagger}$ ) experiments [47]. Arbitrary  $Z$ -rotations are defined virtually by phase shifts in software [45].

### 4. 0-1-2 discriminator error rates

In this subsection, we briefly explain why the limited accuracy of a custom 0 – 1 – 2 discriminator for the IBM backends necessitates an exponential number of circuits (in relation to the number of qubits) that depend on the highly accurate 0 – 1 discriminator for precise fidelity computation.

We build the 0 – 1 – 2 discriminator as follows ([51, 69])

1. Compute the 1 → 2 frequency through narrow-band spectroscopy.
2. Conduct the Rabi experiment to determine the  $\pi$  pulse amplitude for the 1 → 2 transition. The process is as follows: First, apply a 0 → 1  $\pi$  pulse to transition from the  $|0\rangle$  state to the  $|1\rangle$  state. Next, perform a sweep of drive amplitudes at the previously obtained 1 → 2 frequency.
3. Construct three schedules: (i)  $|0\rangle$  schedule: just measure the ground state. (ii)  $|1\rangle$  schedule: apply a 0 → 1  $\pi$  pulse and measure. (iii)  $|2\rangle$  schedule: apply a 0 → 1  $\pi$  pulse, then a 1 → 2  $\pi$  pulse and measure their IQ (In-phase and Quadrature phase components of the measurement signal) data points.
4. Collect data from each schedule, divide it into training and testing sets, and build a Linear discriminant Analysis (LDA) model for discrimination (Fig. 13).

With three centroids, the separatrix is no longer a simple line but rather a curve formed by a combination of two lines. To distinguish between the  $|0\rangle$ ,  $|1\rangle$ , and  $|2\rangle$  states, our model evaluates the position of the IQ point relative to the separatrix and classifies it accordingly. The LDA score (accuracy in correctly classifying the states; 1.0 is exact classification) for this discriminator is 0.873. This is very inaccurate compared to the 0 – 1 discriminator which has a readout assignment error in the range of 0.01 – 0.02.

The inaccuracy described above could affect the results significantly, especially with multiple numbers of qubits, since the error rate in correctly classifying a ternary bit string is roughly the product of error rates for individual qubits. This motivated us to consider an exponential number of circuits where we essentially separate  $|1\rangle$  from  $|2\rangle$  by applying additional  $X_{01}$  gates to the original circuit and using them to find the true  $|1\rangle$  probabilities. It is important to emphasize that there are efforts in building an accurate 0 – 1 – 2 discriminator (such as [52]), which would rule out the requirement of an exponential number of circuits that we currently have.



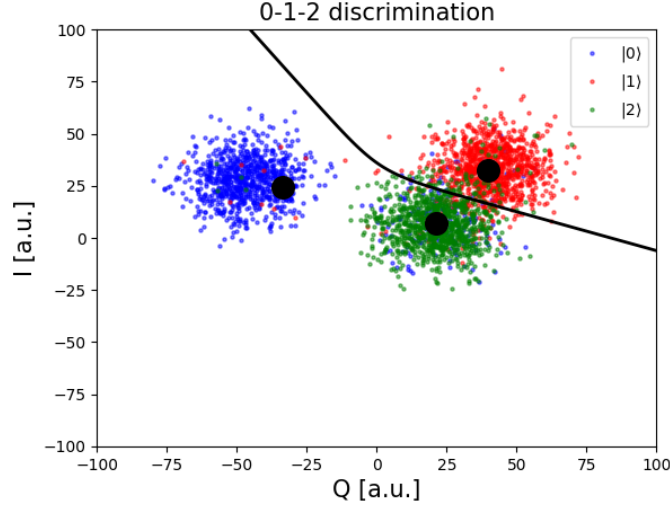


FIG. 13. To discriminate between  $|0\rangle$ ,  $|1\rangle$ , and  $|2\rangle$  states, our model checks where the IQ point lies relative to the separatrix and classifies the point accordingly. This experiment was run on qubit 15 of *ibm nazca*.

### 5. Pulse parameters and gate fidelities

Qutrit	$X_{12}$ amplitude	Anharmonicity	Beta ( $\beta$ )	$X_{12}$ gate error (EPC/2)
1	1.486e-01	-3.4199e+08	2.6827e-01	0.00038 $\pm$ 0.00022
2	1.6537e-01	-3.3948e+08	-1.3157	0.00035 $\pm$ 0.00005
3	2.0118e-01	-3.4274e+08	-3.0499e-01	0.00027 $\pm$ 0.00005

TABLE V. Qutrit gate fidelities (in Error Per Clifford (EPC)) and calibrated parameters of the pulse gates. For  $n = 2$  (both OBC and PBC (Fig. 3, Fig. 7)), qutrits 1 and 2 were used. For  $n = 3$  (Fig. 3), qutrits 1, 2 and 3 were used. For  $n = 4$  (Fig. 5), qutrits 1, 2, 3 and qubit 4 were used (one does not need to calibrate qutrit 4 for the state preparations in interest). Qubits 3, 2, 1 and 4 exist in a single linear chain in that order.

### Appendix E: Parameters for the circuits (OBC and PBC) run on hardware

Circuit diagrams with pulse gates (and 0 – 1 manifold gates) along with the states that they produce are shown below. We refer the reader to the GitHub files ([GitHub repository](#)) for precise parameter values.

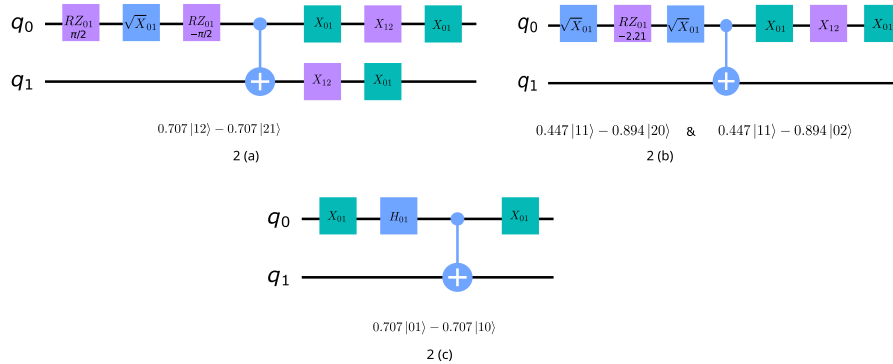


FIG. 14. OBC AKLT ground state circuits for  $n = 2$ . 2(a) captures one of the ground states. 2(b) captures two out of four ground states up to an inversion in the qutrit connectivity list. The Hellinger fidelities of these states are shown in the table I. 2(c) captures the fourth ground state but it can be prepared in 0 – 1 manifold without any qutrit gates, hence can be obtained with 99 – 100% Hellinger fidelity.

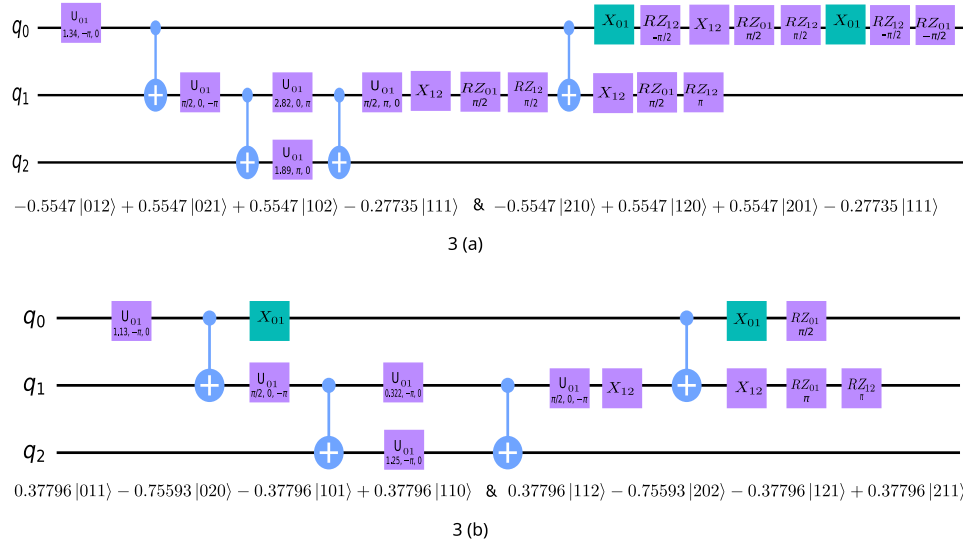


FIG. 15. OBC AKLT ground state circuits for  $n = 3$ . 3(a) captures two out of four ground states up to an inversion in the qutrit connectivity list. 3(b) captures two out of four ground states up to a trivial layer of single qutrit gates taking  $|0\rangle \leftrightarrow |2\rangle$ . For Hellinger fidelity computation, the same set of circuits used for computing the full probability vector of 3(b) suffices to compute the full probability vector of the 3(b) with  $|0\rangle \leftrightarrow |2\rangle$  transformation in the end. The Hellinger fidelities of these states are shown in the table I.

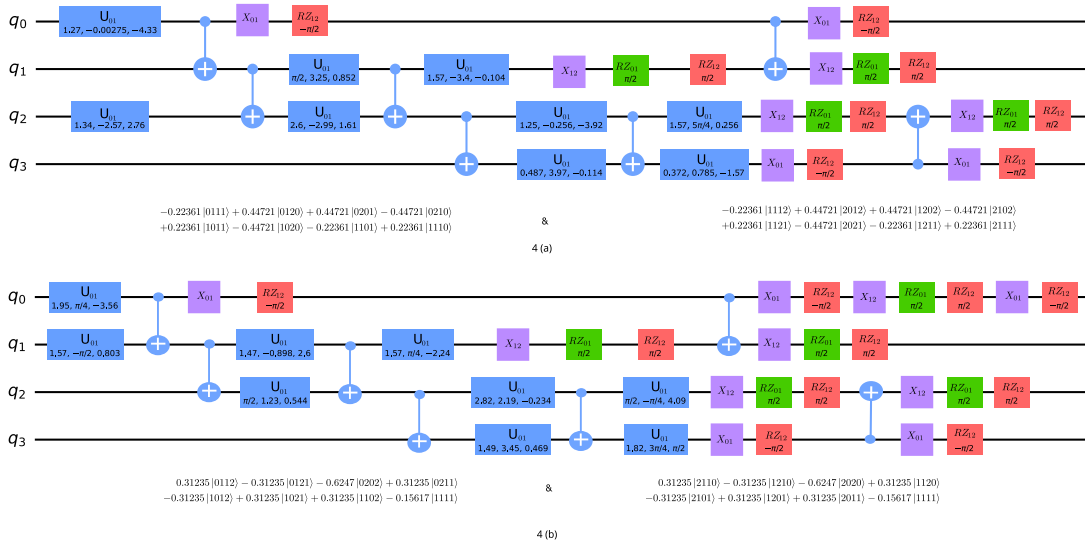


FIG. 16. OBC AKLT ground state circuits for  $n = 4$ . 4(a) captures two out of four ground states up to a trivial layer of single qutrit gates taking  $|0\rangle \leftrightarrow |2\rangle$ . For Hellinger fidelity computation, the same set of circuits used for computing the full probability vector of 4(a) suffices to compute the full probability vector of the 4(a) with  $|0\rangle \leftrightarrow |2\rangle$  transformation in the end. 4(b) captures the other two ground states up to an inversion in the qutrit connectivity list. The Hellinger fidelities of these states are shown in the table I.

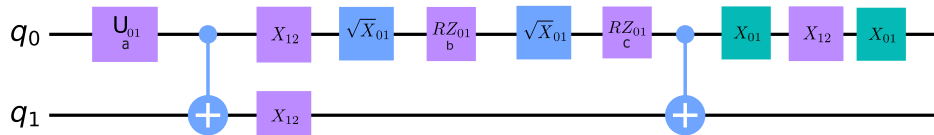


FIG. 17. PBC perturbed AKLT ground state circuits. The  $U_{01}$  gate is the standard  $U$  gate used in qubits-based circuits A. The parameters  $(a, b, c)$  depend on the value of perturbation and can be found in the files in the Github repository attached.

## Appendix F: Phase differences between dominant vector components

### a. Phase shift experiments

There are studies regarding the general state tomography approach for qutrit circuits [70, 71]. These approaches need to be significantly different than qubit state tomography because the number of generators of the  $SU(3)$  group (acting on a qutrit) is 8 and would require around  $8^N$  circuits to fully perform state tomography on an  $N$  qutrit circuit (compare this with  $3^N$  circuits required for an  $N$  qubit state tomography). However, since we know the form of the states Eq. (9), we can focus on just two sets of tomography circuits Fig. 18. These two circuits can be used to compute the (real) phase difference between the ( $|02\rangle$  and  $|11\rangle$ ) components and ( $|20\rangle$  and  $|11\rangle$ ). Let the  $|ij\rangle$ -th component's coefficient be  $a_{ij}$ , then the output probability of  $|00\rangle$  state of the circuit (a) in Fig. 18 is

$$P(|00\rangle) = \frac{|(a_{02} - a_{11}e^{i\phi_s})|^2}{4}, \quad (\text{F1})$$

where  $\phi_s$  is the contribution due to the Stark shifts described earlier.

For circuit (b) in Fig. 18

$$P(|00\rangle) = \frac{|(a_{20} - a_{11}e^{i\phi_s})|^2}{4} \quad (\text{F2})$$

There is no known straightforward relationship between the phase additions in both of these circuits, we correct them separately.

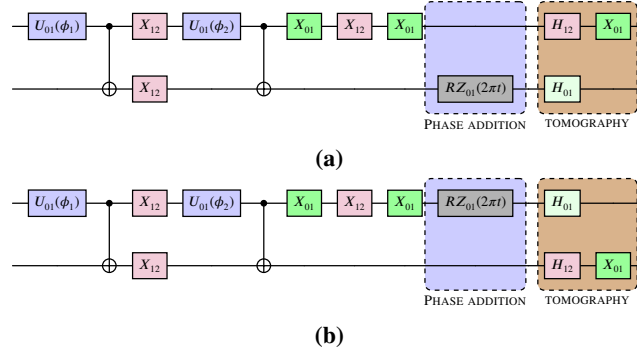


FIG. 18. **Phase shift experiments:** We perform phase shift experiment by introducing a controllable phase  $2\pi t$  ( $t \in [0,1]$ ) between the  $a_{02}$  and  $a_{11}$  components in the circuit (a) and the  $a_{20}$  and  $a_{11}$  components in the circuit (b). Then state tomography analog of qutrits is performed, resulting in the output  $P(00) = \frac{|a_{02} - a_{11}e^{i(\phi + i\phi_s)}|}{4}$  for the circuit (a) and  $P(00) = \frac{|a_{20} - a_{11}e^{i(\phi + i\phi_s)}|}{4}$  for the circuit (b). In the figure,  $\phi$  is the controllable phase and  $\phi_s$  is the contribution from the Stark shift which we wish to correct.

The first set of phase shift experiments was performed by introducing a controllable phase  $2\pi t$  ( $t \in [0,1]$ ) between the  $|02\rangle$  and  $|11\rangle$  components in the circuit (a) of Fig. 18 resulting in plots shown in Fig.19. Then state tomography analog of qutrits is performed, resulting in the output  $P(00) = \frac{|a_{02}-a_{11}e^{i(\phi+i\phi_s)}|^4}{4}$  for the circuit (a). In Fig. 19, we see that the peak occurs at the point where the phase difference between the  $|02\rangle$ ,  $|11\rangle$  components gets canceled by the controlled rotation  $\phi$  and informs us the required phase correction (Fig. 22) for our state.

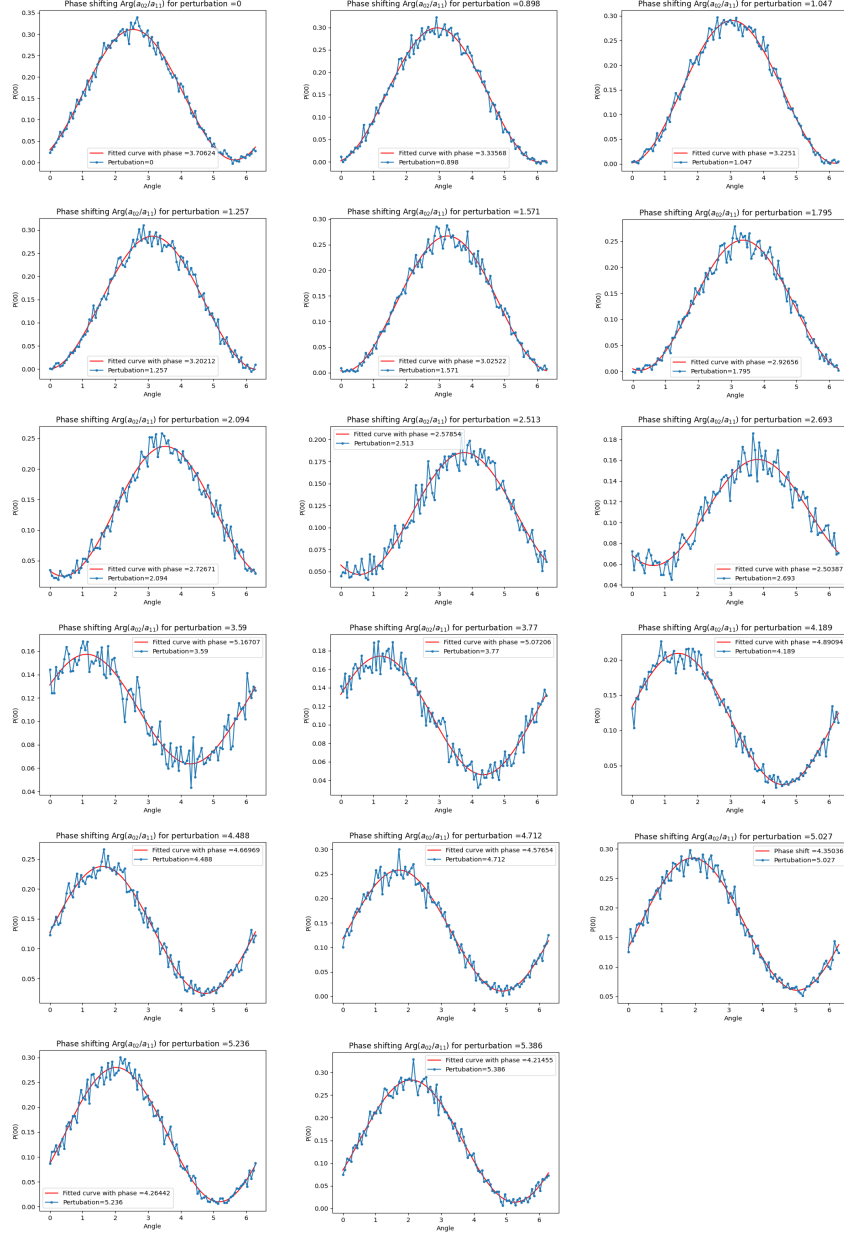


FIG. 19. **Phase shift experiments 1:** Phase shift plots corresponding to ( $|02\rangle$ ,  $|11\rangle$ ) states for all the perturbed ground states (perturbation angle shown in the subplots) are considered in this work.

The second set of phase shift experiments was performed by introducing a controllable phase  $2\pi t$  ( $t \in [0,1]$ ) between the  $|20\rangle$  and  $|11\rangle$  components in the circuit (b) of Fig. 18. Then state tomography is performed, resulting in the output  $P(00) = \frac{|a_{20}-a_{11}e^{i(\phi+i\phi_s)}|^4}{4}$  for the circuit (b). In Fig. 20, we see that the peak occurs at the point where the phase difference between the  $|20\rangle$ ,  $|11\rangle$  components gets canceled by the controlled rotation  $\phi$  and informs us about the exact phase correction (Fig. 22) required for our state.

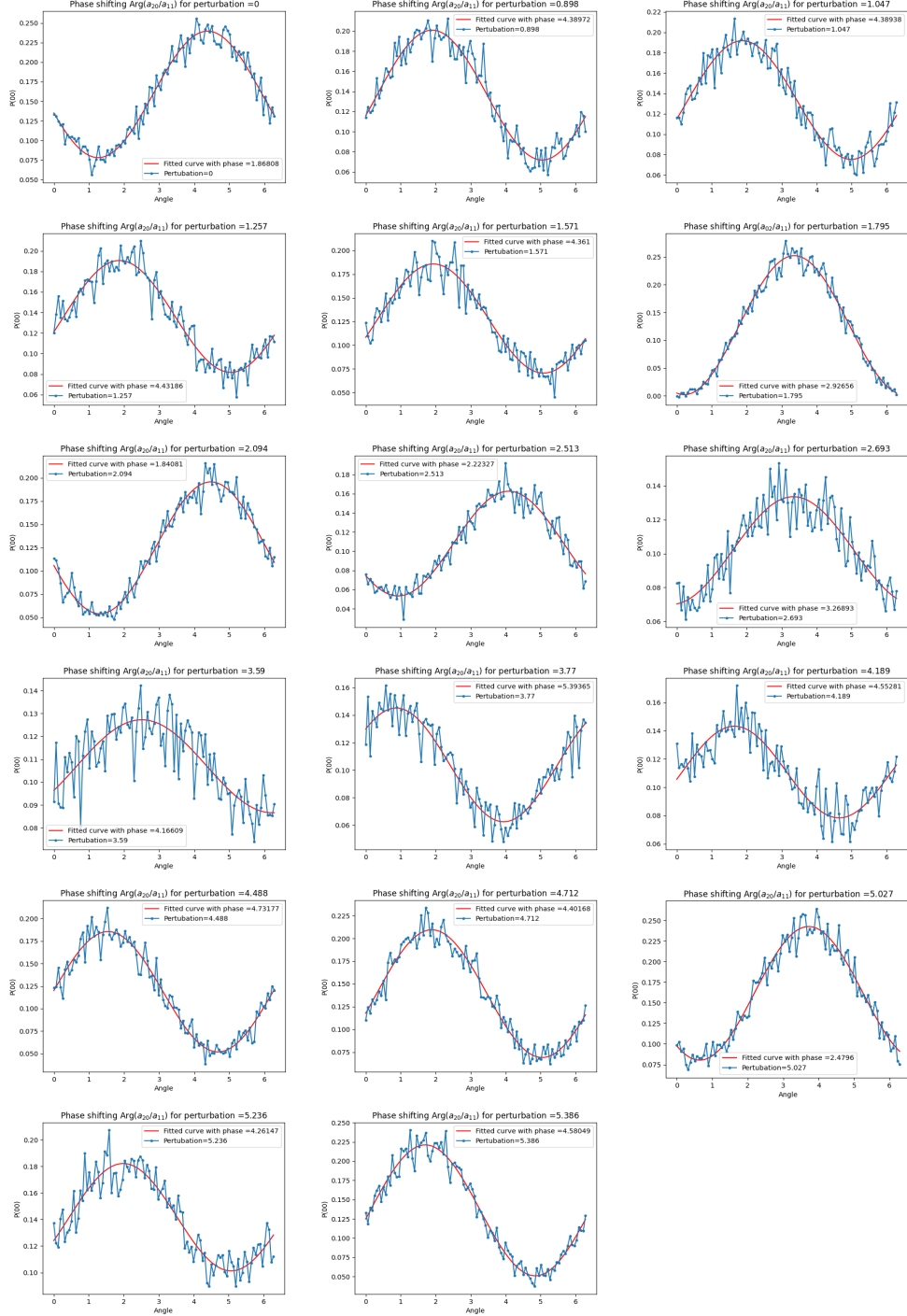


FIG. 20. **Phase shift experiments 2:** Phase shift plots corresponding to ( $|20\rangle$ ,  $|11\rangle$ ) states for all the perturbed ground states (perturbation angle shown in the subplots) are considered in this work.

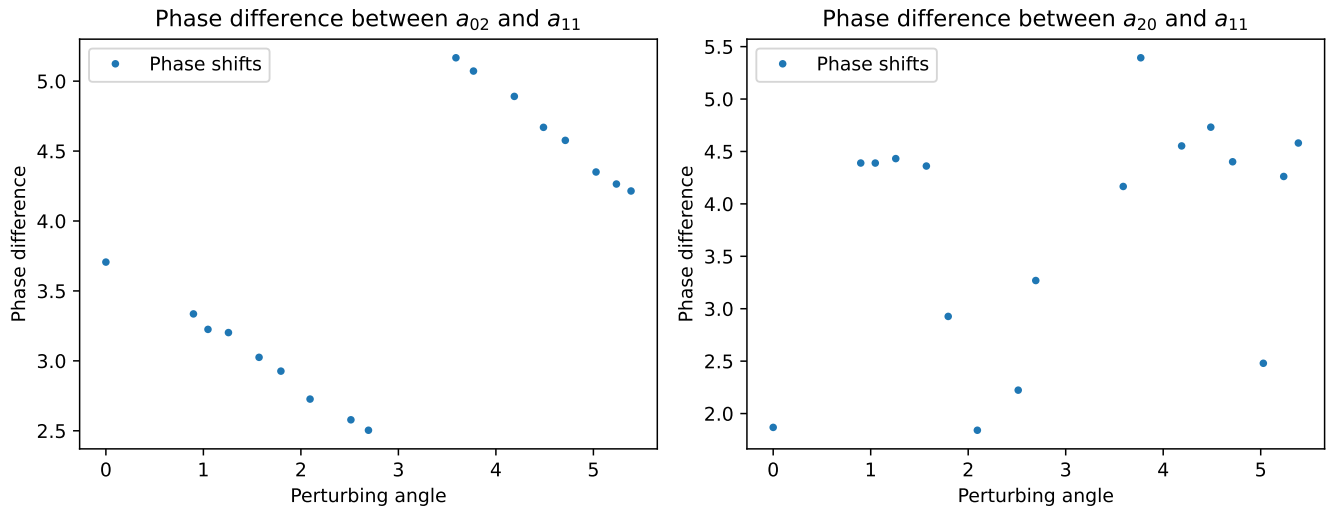


FIG. 21. The phase difference between  $|20\rangle$  or  $|02\rangle$  and  $|11\rangle$  components. (a) The phase difference between  $|02\rangle$  and  $|11\rangle$  components obey a very regular trend for various controlled angle rotations. (b) The phase difference between  $|20\rangle$  and  $|11\rangle$  components depends on the device conditions and fluctuates significantly. Hence, care has to be taken to run these circuits within a single session to get the phase corrections.

It is important to note that the phase shift plots need not necessarily reach their theoretical maximum and minimum owing to imperfect final states (Fidelity  $< 100\%$ ) prepared in the hardware. The hardware data corresponding to these experiments can be found in the [GitHub repository](#) repository attached.

b. Phase correction

For the berry phase computation, the phase shift experiments need to be done for all the perturbing angles corresponding to the partitions we use (See Fig 19, 20). The angle at which the  $P(|00\rangle)$  of the circuit (a or b) is maximum corresponds to the point where  $|02\rangle$  or  $|20\rangle$  and  $|11\rangle$  are in phase. These experiments give us the phase differences that already exist for the state in the absence of the controllable phase addition. Based on the obtained phase differences, one can add a layer of  $RZ_{12}$  gates to add the expected phase to our state Fig. 22. This procedure doesn't affect the fidelities of our ansatz circuit because the additional  $RZ$  gates are all zero duration virtual gates [45] and hence noiseless.

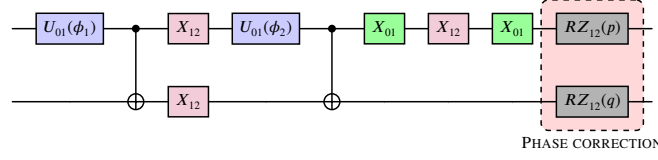


FIG. 22. **Phase correction:** The Fig. 18 provides the phase difference between  $|02\rangle$  and  $|11\rangle$  components (circuit(a)) and  $|20\rangle$  and  $|11\rangle$  (circuit (b)). Using a layer of  $RZ_{12}$  gates, one can introduce the expected phase difference between those components. This correction procedure is noiseless as the added gates in this procedure are all virtual noiseless  $RZ$  rotations.

### Appendix G: Compilation of matrix product states

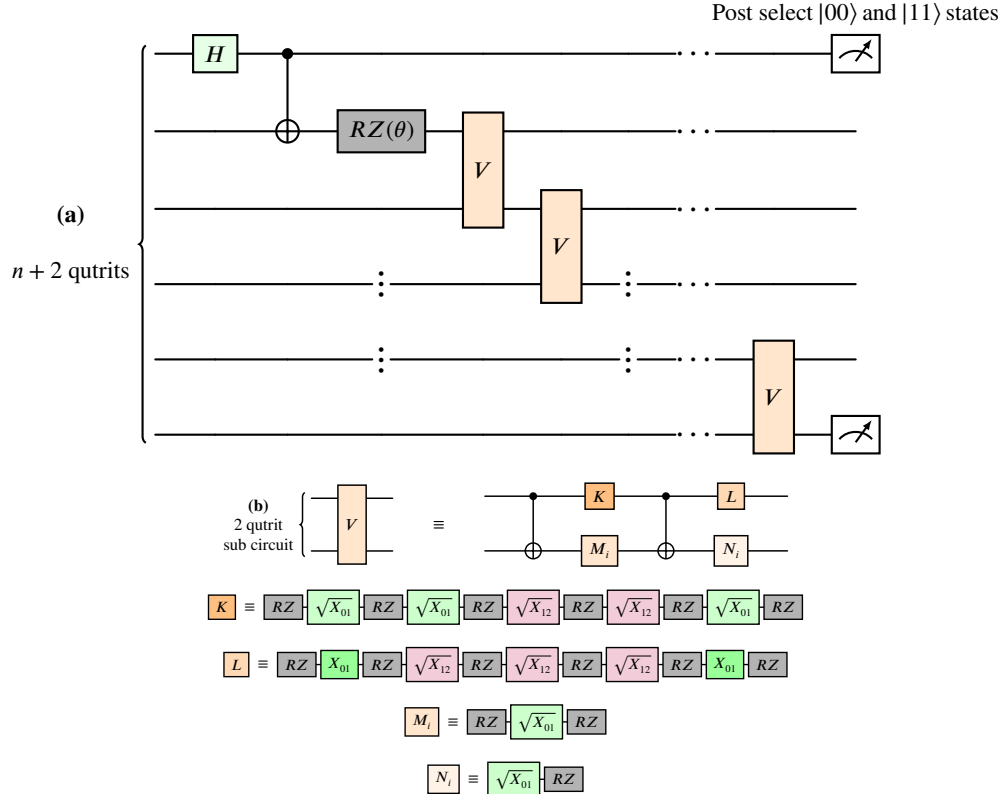


FIG. 23. **Compilation of PBC AKLT ground state.** The compilation shown is in terms of native qutrit gates. An equivalent compilation exists in terms of qubit gates.

To derive scalable circuits to prepare AKLT ground states, we use the encoding of MPS into circuits described in [55]. For PBC AKLT model with perturbation angle,  $\theta$ , the circuit is shown in Fig. 23. The two ancillary qutrits at the edges are measured

and their outcome post-selected to generate the correct classical correlations coming from the periodic boundary.

Note that this method generates a circuit of entangling isometries, denoted by  $V$  in Fig. 23. Each isometry must then be compiled to the native gate set on a device. One way to do this is by embedding the isometry into a unitary and then performing full unitary compilation. However, for a given isometry, there is no canonical choice of embedding, and different embeddings can lead to circuits with vastly different gate counts and, therefore, amounts of noise.

Instead, we find noise-efficient compilations by optimizing an ansatz such that it matches the action of the isometry on the relevant subspace. This is akin to solving a multi-state preparation problem, and avoids full unitary compilation. The cost function we minimize is as follows:

$$C(U) = \sum_j \|U|j\rangle - V|j\rangle\|, \quad (\text{G1})$$

where  $U$  represents an ansatz circuit and  $V$  the target isometry, and  $\{|j\rangle\}$  can be generated by identifying the possible states of the input wires of  $V$  in the circuit. In Fig. 23, the relevant actions of  $V$  that we optimize for are:

$$V|00\rangle = -\sqrt{\frac{1}{3}}|01\rangle - \sqrt{\frac{2}{3}}|12\rangle, \quad (\text{G2})$$

$$V|01\rangle = \sqrt{\frac{2}{3}}|00\rangle + \sqrt{\frac{1}{3}}|11\rangle \quad (\text{G3})$$

For qutrits, the native gate set is described in Appendix A, while for qubits we use the standard CNOT + ZSX gate set available on IBM devices. In both cases our ansatz circuit is built from CNOT gates, with each CNOT dressed with parametrized single site gates on its four wires. We optimize over all possible structures of CNOT gates, starting with structures with the fewest CNOTs. For a given structure, we optimize the single site gates to get the lowest possible value of the cost function. This continues until a structure is found for which the cost function converges below a chosen tolerance.

The optimization of the single site gates can be performed by explicitly parametrizing them and using algorithms like gradient descent or BFGS. In this work, we use the environment tensor method [72] to optimize the gates. Once a solution has been found, the generic single site gates are decomposed into pulses available on the device.

This method is also used to compile the gates necessary for Berry phase computation (see Appendix I). We identify the relevant input states based on the measurement probabilities required for the Hadamard test and ensure that our compilation preserves these probabilities. Since the cost function in Eq. (G1) is sensitive to phases, it is suitable for compiling the Hadamard test circuit.

## Appendix H: Modeling and simulating noise for transmon qutrits

A superconducting qutrit interacting with its environment will thermalize. This thermalization can take place either with or without a loss of energy. In the first case, the qutrit will spontaneously decay from a higher energy state to a lower one, giving off a quantum of energy to the environment. Since the environment has, by definition, many more degrees of freedom than the qutrit, this corresponds to a macrostate with a much larger set of microstates. The resulting increase in entropy can be interpreted as thermalization. We model this behavior with the amplitude damping channel (H1). In the second case, the off diagonal elements of the density matrix will decay while the diagonal elements stay preserved. Therefore, the energy of the qutrit will remain unchanged but its von Neumann entropy will increase, once again allowing it to thermalize. The dephasing channel (H2) is used to model this phenomenon.

We will now heuristically derive the Kraus operators of each channel and then relate their free parameters to experimentally observable  $T_1$  and  $T_2$  times.

### 1. Amplitude damping channel

Amplitude damping of qutrits corresponds to a unitary on the qutrit + environment system with the following action:



$$U |0_q\rangle |0_E\rangle = |0_q\rangle |0_E\rangle \quad (\text{H1})$$

$$U |1_q\rangle |0_E\rangle = \sqrt{p_{\Delta_{0-1}}} |0_q\rangle |\Delta_{E,0-1}\rangle + \sqrt{1-p_{\Delta_{0-1}}} |1_q\rangle |0_E\rangle \quad (\text{H2})$$

$$U |2_q\rangle |0_E\rangle = \sqrt{p_{\Delta_{1-2}}} |1_q\rangle |\Delta_{E,1-2}\rangle + \sqrt{1-p_{\Delta_{1-2}}} |2_q\rangle |0_E\rangle \quad (\text{H3})$$

where  $q$  labels the qutrit, and  $E$  labels the environment.  $|0_E\rangle$  represents the vacuum state of the environment and  $|\Delta_{E,0-1}\rangle$  and  $|\Delta_{E,1-2}\rangle$  label states of the environment with energies corresponding to the  $1 \rightarrow 0$  and  $2 \rightarrow 1$  transitions of the qutrit respectively.

Note that we are ignoring the possibility of a  $2 \rightarrow 0$  transition since a two photon transition is highly suppressed in real transmon devices. At finite temperature, there would also be a possibility of spontaneous excitation, resulting in generalized amplitude damping. However, here we disregard this possibility since the gap between the qutrit levels is much larger than  $k_B T$ , where  $T$  is the operating temperature of the qutrit.

By tracing out the environment, we can derive the quantum channel acting on the qutrit as a result of the amplitude damping:

$$\mathcal{E}_{AD}(\rho) = \text{Tr}_E(U(\rho \otimes |0_E\rangle \langle 0_E|)U^\dagger) = \sum_i K_i \rho K_i^\dagger \quad (\text{H4})$$

where we have assumed that the environment starts in the  $|0_E\rangle$  state and the Kraus operators are defined as  $K_i = \langle i_E | U | 0_E \rangle$ . Since a three level environment suffices to model this interaction, we end up with three Kraus operators, whose matrix elements can be read off from the definition of  $U$  above:

$$K_0 = \begin{bmatrix} 1 & 0 & 0 \\ 0 & \sqrt{1-p_{\Delta_{0-1}}} & 0 \\ 0 & 0 & \sqrt{1-p_{\Delta_{1-2}}} \end{bmatrix}, \quad K_1 = \begin{bmatrix} 0 & \sqrt{p_{\Delta_{0-1}}} & 0 \\ 0 & 0 & 0 \\ 0 & 0 & 0 \end{bmatrix}, \quad K_2 = \begin{bmatrix} 0 & 0 & 0 \\ 0 & 0 & \sqrt{p_{\Delta_{0-1}}} \\ 0 & 0 & 0 \end{bmatrix}$$

## 2. Dephasing channel

In order to suppress the off-diagonal elements of the density matrix, without affecting the diagonal entries, we can probabilistically apply a phase flip. To see this, observe that  $Z_{12}\rho Z_{12}^\dagger$  adds a negative sign to some of the off-diagonal elements but leaves the diagonal invariant. Note that since  $Z_{01}$  and  $Z_{12}$  are sufficient to suppress all off-diagonal terms and  $Z_{02}$  is a second order effect, we will only consider the former two. Therefore, we can model qutrit dephasing with the following map:

$$\mathcal{E}_D(\rho) = p_{0-1} Z_{01} \rho Z_{01}^\dagger + p_{1-2} Z_{12} \rho Z_{12}^\dagger + (1 - p_{0-1} - p_{1-2}) \rho \quad (\text{H5})$$

## 3. Relating noise channels to $T_1$ and $T_2$ times

We model the noise in a qutrit as a composition of amplitude damping and dephasing channels:  $\mathcal{E}_D(\mathcal{E}_{AD}(\rho))$ . Note that the resulting state has  $3 \times 3 = 9$  Kraus operators and 4 free parameters which we must characterize from experiments.

To characterize  $p_{\Delta_{0-1}}$ , we imagine running the following experiment:

1. Initialize the qutrit to  $|0_q\rangle$
2. Apply  $X_{01}$  to excite qutrit to  $|1_q\rangle$
3. Apply noise channel  $k$  times
4. Measure the probability of finding the qutrit in  $|1_q\rangle$

We can analytically work out this probability to be equal to:  $(1 - p_{\Delta_{0-1}})^k$ . Setting this equal to the measured probability would let us solve for  $p_{\Delta_{0-1}}$ . However, note that in experiments we do not have the ability to apply the noise model for a discrete number of times. Instead, we expose the qutrit to noise for a range of durations and find that the probability of measuring it

in  $|1_q\rangle$  afterward decays exponentially. Therefore, we set:  $(1 - p_{\Delta_{0-1}}) = e^{-T/T_1}$ , where  $T_1$  is the decay rate measured from experiments. Similarly, we can characterize  $p_{\Delta_{1-2}}$  by studying the decay of the qutrit from  $|2_q\rangle$  to  $|1_q\rangle$ .

To characterise  $p_{0-1}$  we run the  $T_2$  echo experiment:

1. Initialize the qutrit to  $|0_q\rangle$
2. Apply  $\sqrt{X_{01}}$
3. Apply noise channel  $k$  times
4. Apply  $X_{01}$
5. Apply noise channel  $k$  times
6. Apply  $\sqrt{X_{01}}$
7. Measure the probability of finding the qutrit in  $|0_q\rangle$

This probability can be found analytically to be equal to:  $\frac{1}{2}(1 + (1 - 2p_{0-1})^{2k}(1 - p_{\Delta_{0-1}})^k)$ . Taking the continuous limit, we set:  $(1 - 2p_{0-1}) = e^{-T/T_2}$ . The equivalent experiment for  $p_{1-2}$  involves replacing  $|0_q\rangle$  with  $|1_q\rangle$  and the 0-1 gates with their 1-2 equivalents.

The value of  $T_1$  and  $T_2$  is different for each qutrit on the device. For the purposes of our noise model, we pick typical values of  $100 \mu\text{s}$  and  $75 \mu\text{s}$  for  $T_1$  and  $T_2$  respectively, for both 0 – 1 and 1 – 2 levels. The gate durations of the CNOT gate and native single qutrit gate were chosen to be 500 ns and 40 ns respectively.

#### 4. Tensor network simulation of gate-based noise

In order to simulate the effect of noise in a quantum circuit, we must promote each gate,  $V$ , in the circuit to a superoperator:

$$\Lambda_V = \left( \sum_i K_i^* \otimes K_i \right) \circ (V^* \otimes V) \quad (\text{H6})$$

where  $K_i$  are Kraus operators that depend on measured  $T_1, T_2$  times and the gate time  $T$ . Note that it is helpful to think of  $\Lambda_V$  as a tensor with four indices. For a qutrit, the dimension of each index is three. Our simulator computes the action of this superoperator on a state by contracting two of its indices to those of a density matrix represented as a matrix product operator.

#### Appendix I: Hadamard test for states prepared using post-selection

In this section, we describe a generalized Hadamard test that can be used to compute the overlap of two states prepared using post-selection. Suppose we want to compute the overlap of  $|\phi_t\rangle$  and  $|\psi_t\rangle$  and have circuits  $U_\phi$  and  $U_\psi$  such that:

$$|\phi_t\rangle = \frac{1}{\sqrt{p_0}} \langle 0_a | \phi \rangle + \frac{1}{\sqrt{p_1}} \langle 1_a | \phi \rangle = \frac{1}{\sqrt{p_0}} \langle 0_a | U_\phi | 0_s \rangle | 0_a \rangle + \frac{1}{\sqrt{p_1}} \langle 1_a | U_\phi | 0_s \rangle | 0_a \rangle \quad (\text{I1})$$

$$|\psi_t\rangle = \frac{1}{\sqrt{q_0}} \langle 0_b | \psi \rangle + \frac{1}{\sqrt{q_1}} \langle 1_b | \psi \rangle = \frac{1}{\sqrt{q_0}} \langle 0_b | U_\psi | 0_s \rangle | 0_b \rangle + \frac{1}{\sqrt{q_1}} \langle 1_b | U_\psi | 0_s \rangle | 0_b \rangle, \quad (\text{I2})$$

where the  $s$  labels system register,  $a, b$  label ancilla registers, and  $|0\rangle$  and  $|1\rangle$  represent the all zero and all one state respectively on the labeled register. Note that while the system register is shared between the two states, each state has its own ancilla register. The probabilities of measuring the ancilla register of  $|\phi\rangle$  in the all zero and all one state are represented by  $p_0$  and  $p_1$  respectively. The equivalent quantities for  $|\psi\rangle$  are represented by  $q_0, q_1$ .

The overlap between the two states can be written as:

$$\langle \psi_t | \phi_t \rangle = \frac{1}{\sqrt{p_0 q_0}} \langle \psi | 0_b \rangle \langle 0_a | \phi \rangle + \frac{1}{\sqrt{p_0 q_1}} \langle \psi | 1_b \rangle \langle 0_a | \phi \rangle + \frac{1}{\sqrt{p_1 q_0}} \langle \psi | 0_b \rangle \langle 1_a | \phi \rangle + \frac{1}{\sqrt{p_1 q_1}} \langle \psi | 1_b \rangle \langle 1_a | \phi \rangle. \quad (\text{I3})$$

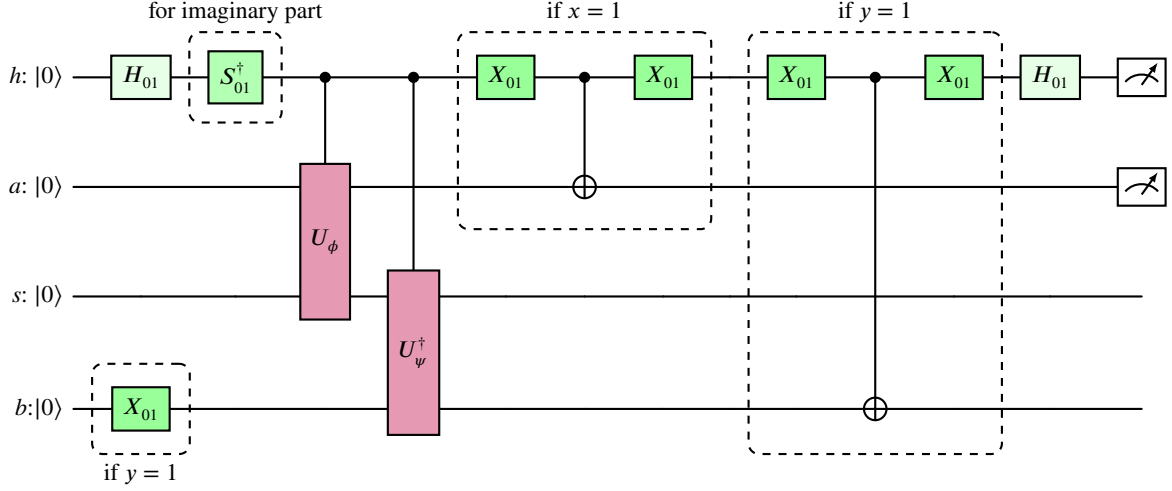


FIG. 24. **Hadamard test for states prepared using post selection.** The real and imaginary parts of  $\langle \psi | y_b \rangle \langle x_a | \phi \rangle$  can be computed by estimating measurement probabilities of the  $h$  and  $a$  registers.

The circuit in Fig. 24 allows us to compute the real and imaginary parts of each of these four terms. Specifically, we can relate each term to certain measurement probabilities of an appropriate circuit. For instance, the circuits used to compute the real part have the following measurement probabilities:

$$\text{prob}(h = 0, a = x) = \frac{1}{4} (1 + p_x + 2\text{Re} \langle \psi | y_b \rangle \langle x_a | \phi \rangle), \quad (14)$$

where  $x, y \in [0, 1]$ . Therefore, estimating these probabilities will allow us to extract the complex overlap.

We can use the modified Hadamard test to compute Berry phase of the PBC AKLT state prepared as described in section VI. Note that for generic states, the controlled- $U$  gates depicted in Fig. 24 will turn into long-range gates, requiring a large number of SWAP gates. However, the ladder structure in Fig. 8 leads to an efficient routing of the Hadamard register and drastically reduces the number of SWAP gates necessary. This routing strategy is depicted in Fig. 25. The long-range CNOT gates at the end of the Hadamard circuits can also be efficiently implemented in cases where the size of the circuit matches the length of a closed loop of qutrits on a two-dimensional device. This is because the CNOT gates only stretch across the edge qutrits and, therefore, we can exploit periodicity to decompose the long-range CNOTs into local CNOTs and SWAP gates that traverse only the edge of the circuit.

The gates necessary to implement these circuits can be compiled using the method described in Appendix G.

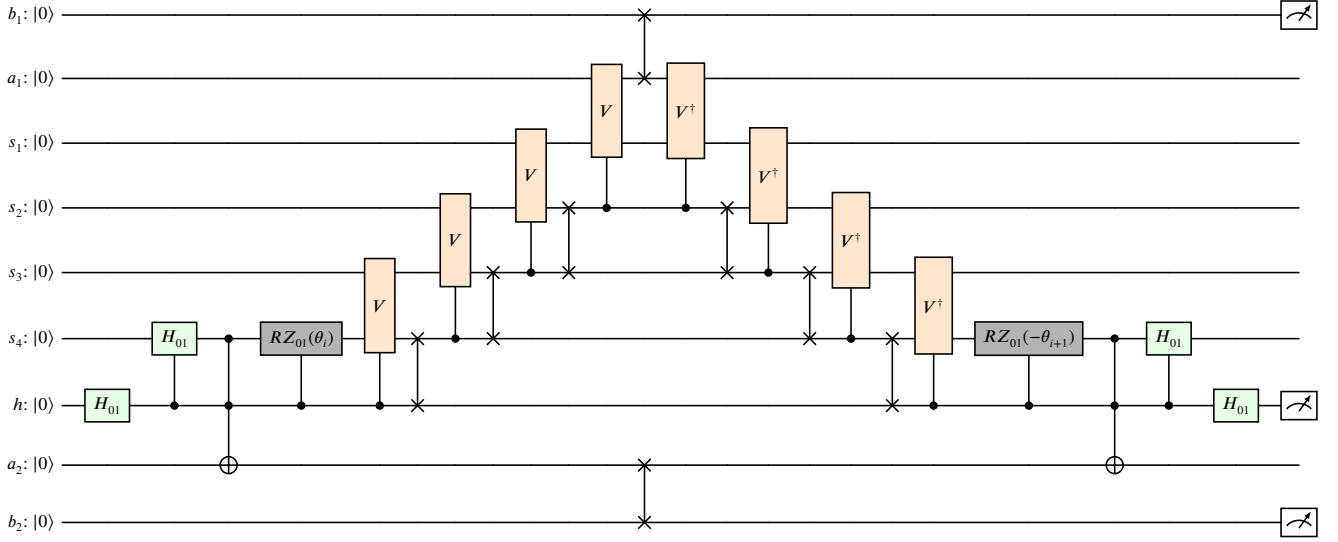


FIG. 25. **Routing of Hadamard register:** Hadamard test circuit for  $\langle GS(\theta_{i+1})|0_b\rangle\langle 0_a|GS(\theta_i)\rangle$ , where  $GS(\theta_i)$  represents the ground state of the PBC AKLT model with perturbation angle,  $\theta_i$ . By exploiting the ladder structure in our state preparation protocol, we find an efficient routing strategy for the Hadamard register that minimizes the number of SWAP gates necessary.